

# Baryon Acoustic Oscillations in the $\text{Ly}\alpha$ forest of BOSS quasars

Nicolás G. Busca<sup>1</sup>, Timothée Delubac<sup>2</sup>, James Rich<sup>2</sup>, Stephen Bailey<sup>3</sup>, Andreu Font-Ribera<sup>3,27</sup>, David Kirkby<sup>4</sup>, J.-M. Le Goff<sup>2</sup>, Matthew M. Pieri<sup>5</sup>, Anže Slosar<sup>6</sup>, Éric Aubourg<sup>1</sup>, Julian E. Bautista<sup>1</sup>, Dmitry Bizyaev<sup>7</sup>, Michael Blomqvist<sup>4</sup>, Adam S. Bolton<sup>8</sup>, Jo Bovy<sup>9</sup>, Howard Brewington<sup>7</sup>, Arnaud Borde<sup>2</sup>, J. Brinkmann<sup>7</sup>, Bill Carithers<sup>3</sup>, Rupert A.C. Croft<sup>10</sup>, Kyle S. Dawson<sup>8</sup>, Garrett Ebelke<sup>7</sup>, Daniel J. Eisenstein<sup>11</sup>, Jean-Christophe Hamilton<sup>1</sup>, Shirley Ho<sup>10</sup>, David W. Hogg<sup>12</sup>, Klaus Honscheid<sup>13</sup>, Khee-Gan Lee<sup>14</sup>, Britt Lundgren<sup>15</sup>, Elena Malanushenko<sup>7</sup>, Viktor Malanushenko<sup>7</sup>, Daniel Margala<sup>4</sup>, Claudia Maraston<sup>5</sup>, Kushal Mehta<sup>16</sup>, Jordi Miralda-Escudé<sup>17,18</sup>, Adam D. Myers<sup>19</sup>, Robert C. Nichol<sup>5</sup>, Pasquier Noterdaeme<sup>20</sup>, Matthew D. Olmstead<sup>8</sup>, Daniel Oravetz<sup>7</sup>, Nathalie Palanque-Delabrouille<sup>2</sup>, Kaikai Pan<sup>7</sup>, Isabelle Pâris<sup>20,28</sup>, Will J. Percival<sup>5</sup>, Patrick Petitjean<sup>20</sup>, N. A. Roe<sup>3</sup>, Emmanuel Rollinde<sup>20</sup>, Nicholas P. Ross<sup>3</sup>, Graziano Rossi<sup>2</sup>, David J. Schlegel<sup>3</sup>, Donald P. Schneider<sup>21,22</sup>, Alaina Shelden<sup>7</sup>, Erin S. Sheldon<sup>6</sup>, Audrey Simmons<sup>7</sup>, Stephanie Snedden<sup>6</sup>, Jeremy L. Tinker<sup>12</sup>, Matteo Viel<sup>23,24</sup>, Benjamin A. Weaver<sup>12</sup>, David H. Weinberg<sup>25</sup>, Martin White<sup>3</sup>, Christophe Yèche<sup>2</sup>, Donald G. York<sup>26</sup>

- <sup>1</sup> APC, Université Paris Diderot-Paris 7, CNRS/IN2P3, CEA, Observatoire de Paris, 10, rue A. Domon & L. Duquet, Paris, France
- <sup>2</sup> CEA, Centre de Saclay, IRFU, F-91191 Gif-sur-Yvette, France
- <sup>3</sup> Lawrence Berkeley National Laboratory, 1 Cyclotron Road, Berkeley, CA 94720, USA
- <sup>4</sup> Department of Physics and Astronomy, University of California, Irvine, CA 92697, USA
- <sup>5</sup> Institute of Cosmology and Gravitation, Dennis Sciama Building, University of Portsmouth, Portsmouth, PO1 3FX, UK
- <sup>6</sup> Bldg 510 Brookhaven National Laboratory, Upton, NY 11973, USA
- <sup>7</sup> Apache Point Observatory, P.O. Box 59, Sunspot, NM 88349, USA
- <sup>8</sup> Department of Physics and Astronomy, University of Utah, 115 S 1400 E, Salt Lake City, UT 84112, USA
- <sup>9</sup> Institute for Advanced Study, Einstein Drive, Princeton, NJ 08540, USA
- <sup>10</sup> Bruce and Astrid McWilliams Center for Cosmology, Carnegie Mellon University, Pittsburgh, PA 15213, USA
- <sup>11</sup> Harvard-Smithsonian Center for Astrophysics, Harvard University, 60 Garden St., Cambridge MA 02138, USA
- <sup>12</sup> Center for Cosmology and Particle Physics, New York University, New York, NY 10003, USA
- <sup>13</sup> Department of Physics and Center for Cosmology and Astro-Particle Physics, Ohio State University, Columbus, OH 43210, USA
- <sup>14</sup> Max-Planck-Institut für Astronomie, Königstuhl 17, D69117 Heidelberg, Germany
- <sup>15</sup> Department of Astronomy, University of Wisconsin, 475 North Charter Street, Madison, WI 53706, USA
- <sup>16</sup> Steward Observatory, University of Arizona, 933 N. Cherry Ave., Tucson, AZ 85721, USA
- <sup>17</sup> Institució Catalana de Recerca i Estudis Avançats, Barcelona, Catalonia
- <sup>18</sup> Institut de Ciències del Cosmos, Universitat de Barcelona/IEEC, Barcelona 08028, Catalonia
- <sup>19</sup> Department of Physics and Astronomy, University of Wyoming, Laramie, WY 82071, USA
- <sup>20</sup> Université Paris 6 et CNRS, Institut d'Astrophysique de Paris, 98bis blvd. Arago, 75014 Paris, France
- <sup>21</sup> Department of Astronomy and Astrophysics, The Pennsylvania State University, University Park, PA 16802, USA
- <sup>22</sup> Institute for Gravitation and the Cosmos, The Pennsylvania State University, University Park, PA 16802, USA
- <sup>23</sup> INAF, Osservatorio Astronomico di Trieste, Via G. B. Tiepolo 11, 34131 Trieste, Italy
- <sup>24</sup> INFN/National Institute for Nuclear Physics, Via Valerio 2, I-34127 Trieste, Italy.
- <sup>25</sup> Department of Astronomy, Ohio State University, 140 West 18th Avenue, Columbus, OH 43210, USA
- <sup>26</sup> Department of Astronomy and Astrophysics and the Enrico Fermi Institute, The University of Chicago, 5640 South Ellis Avenue, Chicago, Illinois, 60615, USA
- <sup>27</sup> Institute of Theoretical Physics, University of Zurich, 8057 Zurich, Switzerland
- <sup>28</sup> Departamento de Astronomía, Universidad de Chile, Casilla 36-D, Santiago, Chile

Received November 13th, 2012; accepted February 4th, 2013

## ABSTRACT

We report a detection of the baryon acoustic oscillation (BAO) feature in the three-dimensional correlation function of the transmitted flux fraction in the  $\text{Ly}\alpha$  forest of high-redshift quasars. The study uses 48,640 quasars in the redshift range  $2.1 \leq z \leq 3.5$  from the Baryon Oscillation Spectroscopic Survey (BOSS) of the third generation of the Sloan Digital Sky Survey (SDSS-III). At a mean redshift  $z = 2.3$ , we measure the monopole and quadrupole components of the correlation function for separations in the range  $20h^{-1}\text{Mpc} < r < 200h^{-1}\text{Mpc}$ . A peak in the correlation function is seen at a separation equal to  $(1.01 \pm 0.03)$  times the distance expected for the BAO peak within a concordance  $\Lambda\text{CDM}$  cosmology. This first detection of the BAO peak at high redshift, when the universe was strongly matter dominated, results in constraints on the angular diameter distance  $D_A$  and the expansion rate  $H$  at  $z = 2.3$  that, combined with priors on  $H_0$  and the baryon density, require the existence of dark energy. Combined with constraints derived from Cosmic Microwave Background (CMB) observations, this result implies  $H(z = 2.3) = (224 \pm 8)\text{km s}^{-1}\text{Mpc}^{-1}$ , indicating that the time derivative of the cosmological scale parameter  $\dot{a} = H(z = 2.3)/(1 + z)$  is significantly greater than that measured with BAO at  $z \sim 0.5$ . This demonstrates that the expansion was decelerating in the range  $0.7 < z < 2.3$ , as expected from the matter domination during this epoch. Combined with measurements of  $H_0$ , one sees the pattern of deceleration followed by acceleration characteristic of a dark-energy dominated universe.

**Key words.** cosmology,  $\text{Ly}\alpha$  forest, large scale structure, dark energy

## 1. Introduction

Baryon acoustic oscillations (BAO) in the pre-recombination universe have striking effects on the anisotropies of the Cosmic Microwave Background (CMB) and on the large scale structure (LSS) of matter (Weinberg et al. (2012) and references therein). The BAO effects were first seen in the series of peaks in the CMB angular power spectrum (de Bernardis et al., 2000). Subsequently, the BAO relic at redshift  $z \sim 0.3$  was seen (Eisenstein et al., 2005; Cole et al., 2005) as a peak in the galaxy-galaxy correlation function at a co-moving distance corresponding to the sound horizon at recombination. For the WMAP7 cosmological parameters (Komatsu et al., 2011), the expected comoving scale of the BAO peak is  $r_s = 153$  Mpc, with an uncertainty of  $\approx 1\%$ .

The BAO peak in the correlation function at a redshift  $z$  appears at an angular separation  $\Delta\theta = r_s/(1+z)D_A(z)$  and at a redshift separation  $\Delta z = r_s H(z)/c$ , where  $D_A$  and  $H$  are the angular distances and expansion rates. Measurement of the peak position at any redshift thus constrains the combinations of cosmological parameters that determine  $r_s H$  and  $r_s/D_A$ . While the possibility of measuring both combinations is beginning to be exploited (Chuang & Wang, 2012; Xu et al., 2012), most present measurements have concentrated on the combination  $D_V \equiv [(1+z)^2 D_A^2 c z / H]^{1/3}$ , which determines the peak position for an isotropic distribution of galaxy pairs and an isotropic clustering strength. The “BAO Hubble diagram”,  $D_V/r_s$  vs.  $z$ , now includes the Sloan Digital Sky Survey (SDSS) measurement (Eisenstein et al., 2005) updated to the DR7 (Abazajian et al., 2009) sample and combined with 2dF data (Percival et al., 2010), the 6dF point at  $z = 0.1$  (Beutler et al., 2011), the WiggleZ points at  $(0.4 < z < 0.8)$  (Blake et al., 2011a), and a reanalysis of the SDSS DR7 sample that uses reconstruction (Eisenstein et al., 2007; Padmanabhan et al., 2009) to sharpen the precision of the BAO measurement (Padmanabhan et al., 2012; Mehta et al., 2012). Recently, the Baryon Oscillation Spectroscopic Survey (BOSS; Dawson et al. 2013) of SDSS-III (Eisenstein et al., 2011) has added a precise measurement at  $z \sim 0.57$  (Anderson et al., 2012). BOSS has also reported a measurement of  $D_A(z = 0.55)/r_s$  based on the BAO structure in the angular power spectrum of galaxies (Seo et al., 2012).

In this paper, we present an observation of the BAO peak at  $z \sim 2.3$  found in the flux correlation function of the Ly $\alpha$  forest of BOSS quasars. This is the first such observation at a redshift where the expansion dynamics is matter-dominated,  $z > 0.8$ . The possibility of such a measurement was suggested by McDonald (2003) and White (2003) and first studied in detail by McDonald & Eisenstein (2007). While the galaxy BAO measurements are most sensitive to  $D_V \propto D_A^{2/3} H^{-1/3}$ , the Ly $\alpha$  flux transmission is more sensitive to peculiar velocity gradient effects, which enhance redshift distortions and shift our sensitivity to the expansion rate. As we shall show below, the most accurately measured combination from the Ly $\alpha$  forest BAO peak is  $\propto D_A^{0.2} H^{-0.8}$ , and the present BOSS data set allows us to determine its value to a precision of 3.5%. Combining this result with constraints from CMB observations allows us to deduce the value of  $H(z = 2.3)$  accurate to 4%. Comparing our results with measurements of  $H_0$  and of  $H(0.2 < z < 0.8)$  reveals the expected sequence of deceleration and acceleration in models with dark energy.

The last decade has seen increasing use of Ly $\alpha$  absorption to investigate large scale structure. The number of quasars in early studies (Croft et al., 1999; McDonald et al., 2000; Croft et al., 2002; Viel et al., 2004; McDonald et al., 2006) was enough only

to determine the Ly $\alpha$  absorption correlation along individual lines of sight. With the BOSS project the surface density of quasars is sufficient to probe the full three-dimensional distribution of neutral hydrogen. A study using the first 10,000 BOSS quasars was presented by Slosar et al. (2011). This sample provided clear evidence for the expected long-range correlations, including the redshift-space distortions due to the gravitational growth of structure. With the SDSS data release DR9 (Ahn et al., 2012), we now have  $\sim 60,000$  quasars at  $z \sim 2.3$  (Pâris et al., 2012), with a high enough surface density to observe the BAO peak.

The use of Ly $\alpha$  absorption to trace matter has certain interesting differences from the use of galaxies. Galaxy surveys provide a catalog of positions in redshift space that correspond to points of high over-densities. On the other hand, the forest region of a quasar spectrum provides a complete mapping of the absorption over a  $\sim 400 h^{-1}$  Mpc (comoving) range starting about  $100 h^{-1}$  Mpc in front of the quasar (so as to avoid the necessity of modeling the quasar’s Ly $\alpha$  emission line). To the extent that quasar lines of sight are random, a large collection of quasars can provide a nearly unbiased sample of points where the absorption is measured. Cosmological simulations (Cen et al., 1994; Petitjean et al., 1995; Zhang et al., 1995; Hernquist et al., 1996; Miralda-Escudé et al., 1996; Theuns et al., 1998) indicate that most of the Ly $\alpha$  absorption is due to cosmic filamentary structures with overdensities of order one to ten, much lower than the overdensities of virialized halos sampled by galaxies. These simulations have also indicated that, on large scales, the mean Ly $\alpha$  absorption is a linear tracer of the mass overdensity (Croft et al., 1997, 1998; Weinberg et al., 1998; McDonald et al., 2000; McDonald, 2003), implying a relation of the power spectrum of the measured absorption to that of the underlying mass fluctuations. Finally, the forest is observable in a redshift range inaccessible to current large galaxy surveys and where theoretical modeling is less dependent on non-linear effects in cosmological structure formation. These factors combine to make Ly $\alpha$  absorption a promising tracer of mass that is complementary to galaxy tracers.

With Ly $\alpha$  forest measurements along multiple sightlines, one can attempt to reconstruct the underlying 3-dimensional mass density field (Nusser & Haehnelt, 1999; Pichon et al., 2001; Gallerani et al., 2011), from which one can investigate topological characteristics (Caucci et al., 2008) or the power spectrum (Kitaura et al., 2012). However, the BOSS sample is fairly sparse, with a typical transverse sightline separation  $\sim 15 h^{-1}$  Mpc (comoving), and the signal-to-noise ratio in individual spectra is low (see Fig. 2 below), which makes it poorly suited to such reconstruction techniques. In this paper we take the more direct approach of measuring the BAO feature in the correlation function of transmitted flux fraction (the ratio of the observed flux to the flux expected in the absence of absorption).

The use of the Ly $\alpha$  forest is handicapped by the fact that not all fluctuations of the transmitted flux fraction are due to fluctuations of the density of hydrogen. Because the neutral hydrogen density is believed to be determined by photo-ionization equilibrium with the flux of UV photons from stars and quasars, variations of the UV flux may contribute to fluctuations of the transmitted flux (Worseck & Wisotzki, 2006). In addition, hydrogen can be self-shielded to ionizing photons, leading to much higher neutral fractions and damping wings in strong absorption systems (Font-Ribera et al., 2012b). Metals present in the intergalactic medium provide additional absorption superimposed on the Ly $\alpha$  absorption (Pieri et al., 2010). A further complication results from the fact that the flux correlation function uses the

fluctuations of the transmitted flux about its mean value; this requires an estimate of the product of the mean absorption (as a function of absorber redshift) and the unabsorbed flux for individual quasars (Le Goff et al., 2011).

All of these complications are important for a complete understanding of the statistics of the Ly $\alpha$  forest. Fortunately, they are not expected to produce a sharp peak-like feature in the correlation function, so the interpretation of a peak as due to BAO should give robust constraints on the cosmological parameters.

The BOSS collaboration has performed three independent analyses to search for BAO in Ly $\alpha$  forest. This paper presents two of them, both of which aim to analyze the forest using simple procedures at the expense of some loss of sensitivity. The third analysis, with the goal of an optimal measurement of the flux correlation function with a more complex method, is described in a separate publication (Slosar et al., 2013).

Our methods are tested extensively on a set of detailed mock catalogs of the BOSS Ly $\alpha$  forest data set. These mock catalogs, which use the method presented by Font-Ribera et al. (2012a), will be described in detail in a forthcoming public release paper (S. Bailey et al., in preparation). In addition, the BOSS collaboration have also released a fiducial version of the DR9 Ly $\alpha$  forest spectra (Lee et al., 2012b), with various per-object products including masks, continua, and noise correction vectors designed to aid in Ly $\alpha$  forest analysis. While our analyses implement their own sample selection criteria and continuum determination procedures, we have also applied our measurement to this Lee et al. (2012b) sample.

This paper is organized as follows. Section 2 presents the BOSS quasar sample used in this analysis and the procedure used to produce the quasar spectra. Section 3 describes the analysis to measure the correlation function. Section 4 derives the monopole and quadrupole components of the correlation function and determines the significance of the peak observed in these functions at the BAO scale. The cosmological implications of our detection of a BAO peak are discussed in Section 5. Finally, Appendix A provides a brief description of the mock spectra used to test our methodology and Appendix B shows the result of our BAO measurement applied to the BOSS Ly $\alpha$  sample of Lee et al. (2012b).

## 2. The BOSS quasar sample and data reduction

The BOSS project (Dawson et al., 2013) of SDSS-III (Eisenstein et al., 2011) is obtaining the spectra of  $\sim 1.6 \times 10^6$  luminous galaxies and  $\sim 150,000$  quasars. The project uses upgraded versions of the SDSS spectrographs (Smee et al., 2012) mounted on the Sloan 2.5-meter telescope (Gunn et al., 2006) at Apache Point, New Mexico. BOSS galaxy and quasar spectroscopic targets are selected using algorithms based primarily on photometry from the SDSS camera (Gunn et al., 1998; York et al., 2000) in the *ugriz* bands (Fukugita et al., 1996; Smith et al., 2002) reduced and calibrated as described by Stoughton et al. (2002), Pier et al. (2003), and Padmanabhan et al. (2008). Targets are assigned to fibers appropriately positioned in the  $3^\circ$  diameter focal plane according to a specially designed tiling algorithm (Blanton et al., 2003). Fibers are fixed in place by a pierced metal plate drilled for each observed field and fed to one of two spectrographs. Each exposed plate generates 1,000 spectra covering wavelengths of 360 to 1000 nm with a resolving power ranging from 1500 to 3000 (Smee et al., 2012). A median of 631 of these fibers are assigned to galactic targets and 204 to quasar targets. The BOSS spectroscopic targets are observed in dark and gray time,

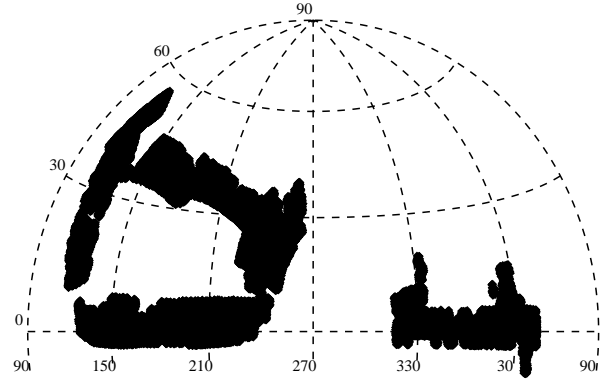


**Fig. 1.** Hammer-Aitoff projection in equatorial coordinates of the BOSS DR9 footprint. The observations cover  $\sim 3000 \text{ deg}^2$ .

while the bright-time is used by other SDSS-III surveys (see Eisenstein et al. 2011).

The quasar spectroscopy targets are selected from photometric data with a combination of algorithms (Richards et al. 2009; Yèche et al. 2009; Kirkpatrick et al. 2011; Bovy et al. 2011; Palanque-Delabrouille et al. 2011; for a summary, see Ross et al. (2012)). The algorithms use SDSS fluxes and, for SDSS Stripe 82, photometric variability. When available, we also use data from non-optical surveys (Bovy et al., 2012): the GALEX survey (Martin et al., 2005) in the UV; the UKIDSS survey (Lawrence et al., 2007) in the NIR, and the FIRST survey (Becker et al., 1995) in the radio.

The quasar spectroscopy targets are divided into two samples “CORE” and “BONUS”. The CORE sample consists of 20 quasar targets per square degree selected from SDSS photometry with a uniform algorithm, for which the selection efficiency for  $z > 2.1$  quasars is  $\sim 50\%$ . The selection algorithm for the CORE sample (Bovy et al., 2011) was fixed at the end of the first year of the survey, thus making it useful for studies that require a uniform target selection across the sky. The BONUS sample was chosen from a combination of algorithms with the purpose of increasing the density on the sky of observed quasars beyond that of the CORE sample. The combined samples yield a mean density of identified quasars of  $15 \text{ deg}^{-2}$  with a maximum of  $20 \text{ deg}^{-2}$ , mostly in zones where photometric variability, UV, and/or NIR data are available. The combined BONUS plus CORE sample can be used for Ly $\alpha$  BAO studies, which require the highest possible quasar density in a broad sky area but are insensitive to the uniformity of the quasar selection criteria because the structure being mapped is in the foreground of these quasar back-lights.

The data presented here consist of the DR9 data release (Ahn et al., 2012) covering  $\sim 3000 \text{ deg}^2$  of the sky shown in figure 1. These data cover about one-third of the ultimate BOSS footprint.

The data were reduced with the SDSS-III pipeline as described in Bolton et al. (2012). Typically four exposures of 15 minutes were co-added in pixels of wavelength width  $\sim 0.09 \text{ nm}$ . Besides providing flux calibrated spectra, the pipeline provided preliminary object classifications (galaxy, quasar, star) and redshift estimates.

The spectra of all quasar targets were visually inspected, as described in Pâris et al. (2012), to correct for misidentifications or inaccurate redshift determinations and to flag

broad absorption lines (BAL). Damped Ly $\alpha$  troughs are visually flagged, but also identified and characterized automatically (Noterdaeme et al., 2012). The visual inspection of DR9 confirms 60,369 quasars with  $2.1 \leq z_q \leq 3.5$ . In order to simplify the analysis of the Ly $\alpha$  forest, we discarded quasars with visually identified BALs and DLAs, leaving 48,640 quasars.

For the measurement of the flux transmission, we use the rest-frame wavelength interval

$$104.5 < \lambda_{\text{rf}} < 118.0 \text{ nm} . \quad (1)$$

The range is bracketed by the Ly $\alpha$  and Ly $\beta$  emission lines at 121.6 and 102.5 nm. The limits are chosen conservatively to avoid problems of modeling the shapes of the two emission lines and to avoid quasar proximate absorbers. The absorber redshift,  $z = \lambda/\lambda_{\text{Ly}\alpha} - 1$ , is in the range  $1.96 < z < 3.38$ . The lower limit is set by the requirement that the observed wavelength be greater than 360 nm below which the system throughput is less than 10% its peak value. The upper limit comes from the maximum quasar redshift of 3.5, beyond which the BOSS surface density of quasars is not sufficient to be useful. The distribution of absorber redshift is shown in figure 2 (top panel). When given the weights used for the calculation of the correlation function (section 3.3), the absorbers have a mean redshift of  $\langle z \rangle = 2.31$ .

For the determination of the correlation function, we use “analysis pixels” that are the flux average over three adjacent pipeline pixels. Throughout the rest of this paper, “pixel” refers to analysis pixels unless otherwise stated. The effective width of these pixels is  $210 \text{ km s}^{-1}$ , i.e. an observed-wavelength width  $\sim 0.27 \text{ nm} \sim 2 \text{ h}^{-1} \text{ Mpc}$ . The total sample of 48,640 quasars thus provides  $\sim 8 \times 10^6$  measurements of Ly $\alpha$  absorption over a total volume of  $\sim 20 \text{ h}^{-3} \text{ Gpc}^3$ .

Figure 2 (bottom panel) shows the distribution of the signal-to-noise ratio for pixels averaged over the forest region. The relatively modest mean value of 5.17 reflects the exposure times necessary to acquire such a large number of spectra.

In addition to the BOSS spectra, we analyzed 15 sets of mock spectra that were produced by the methods described in appendix A. These spectra do not yet reproduce all of the characteristics of the BOSS sample, but they are nevertheless useful for a qualitative understanding of the shape of the measured correlation function. More importantly, they are useful for understanding the detectability of a BAO-like peak and the precision of the measurement of its position.

### 3. Measurement of the correlation function

The flux correlation function can be determined through a simple two-step process. In the first step, for each pixel in the forest region (equation 1) of quasar  $q$ , the measured flux  $f_q(\lambda)$  at observed wavelength  $\lambda$  is compared with the mean expected flux,  $C_q(\lambda)\bar{F}(z)$ , thus defining the “delta field”:

$$\delta_q(\lambda) = \frac{f_q(\lambda)}{C_q(\lambda)\bar{F}(z)} - 1 . \quad (2)$$

Here,  $C_q(\lambda)$  is the unabsorbed flux (the so-called “continuum”) and  $\bar{F}(z)$  is the mean transmitted fraction at the HI absorber redshift. The quantities  $\lambda$  and  $z$  in equation 2 are not independent but related via  $z = \lambda/\lambda_{\text{Ly}\alpha} - 1$ .

Figure 3 shows an example of an estimation for  $C_q(\lambda)$  (blue line) and  $C_q\bar{F}$  (red line). Our two methods for estimating  $C_q$  and  $\bar{F}$  are described in sections 3.1 and 3.2.

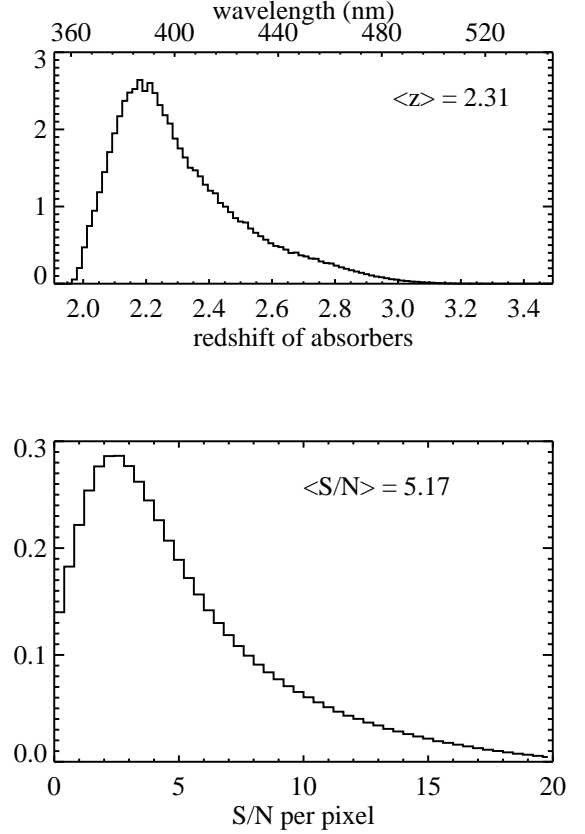


**Fig. 2.** Top: weighted distribution of absorber redshifts used in the calculation of the correlation function in the distance range  $80 \text{ h}^{-1} \text{ Mpc} < r < 120 \text{ h}^{-1} \text{ Mpc}$ . Bottom: distribution of signal-to-noise ratio for analysis pixels (triplets of pipeline pixels) averaged over the forest region.

In the second step, the correlation function is calculated as a weighted sum of products of the deltas:

$$\hat{\xi}_A = \sum_{ij \in A} w_{ij} \delta_i \delta_j / \sum_{ij \in A} w_{ij} , \quad (3)$$

where the  $w_{ij}$  are weights and each  $i$  or  $j$  indexes a measurement on a quasar  $q$  at wavelength  $\lambda$ . The sum over  $(i, j)$  is understood to run over all pairs of pixels of all pairs of quasars within  $A$  defining a region in space of pixel separations,  $\mathbf{r}_i - \mathbf{r}_j$ . The region  $A$  is generally defined by a range  $r_{\min} < r < r_{\max}$  and  $\mu_{\min} < \mu < \mu_{\max}$  with:

$$r = |\mathbf{r}_i - \mathbf{r}_j| \quad \mu = \frac{(\mathbf{r}_i - \mathbf{r}_j)_{\parallel}}{r} \quad (4)$$

where  $(\mathbf{r}_i - \mathbf{r}_j)_{\parallel}$  is the component along the line of sight. Separations in observational pixel coordinates (ra, dec, z) are transformed to  $(r, \mu)$  in units of  $\text{h}^{-1} \text{ Mpc}$  by using a  $\Lambda$ CDM fiducial cosmology with matter and vacuum densities of

$$(\Omega_M, \Omega_\Lambda) = (0.27, 0.73) . \quad (5)$$

In the sum (3), we exclude pairs of pixels from only one quasar to avoid the correlated errors in  $\delta_i$  and  $\delta_j$  coming from the estimate of  $C_q$ . Note that the weights in eq. 3 are set to zero for pixels flagged by the pipeline as having problems due, e.g., to sky emission lines or cosmic rays.

A procedure for determining  $\xi$  is defined by its method for estimating the expected flux  $C_q \bar{F}$  and by its choice of weights,  $w_{ij}$ . The two methods described here use the same technique to calculate weights but have different approaches to estimate  $C_q \bar{F}$ . We will see that the two methods produce correlation functions that have no significant differences. However, the two independent codes were invaluable for consistency checks throughout the analysis.

The two methods were “blind” to the extent that many of the procedures were defined during tests either with mock data or with the real data in which we masked the region of the peak in the correlation function. Among those aspects fixed in this way were the quasar sample, the continuum determination, the weighting, the extraction of the monopole and quadrupole correlation function and the determination of the peak significance (section 4). This early freezing of procedures resulted in some that are suboptimal but which will be improved in future analyses. We note, however, that the procedures used to extract cosmological information (section 5) were decided on only after de-masking the data.

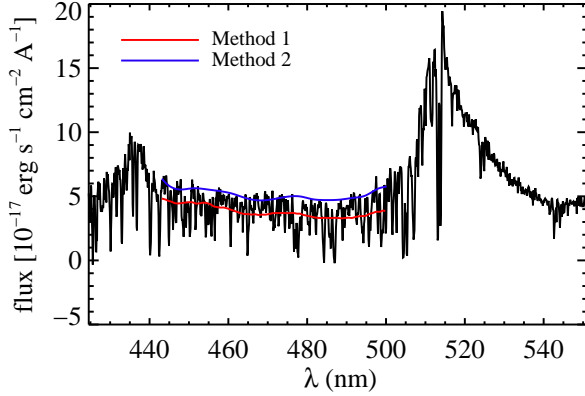


**Fig. 3.** An example of a BOSS quasar spectrum of redshift 3.239. The red and blue lines cover the forest region used here,  $104.5 < \lambda_{\text{rf}} < 118.0$ . This region is sandwiched between the quasar’s Ly $\beta$  and Ly $\alpha$  emission lines respectively at 435 and 515 nm. The blue line is an estimate of the continuum (unabsorbed flux) by method 2 and the red line is the estimate of the product of the continuum and the mean absorption by method 1.

### 3.1. Continuum fits, method 1

Both methods for estimating the product  $C_q \bar{F}$  assume that  $C_q$  is, to first approximation, proportional to a universal quasar spectrum that is a function of rest-frame wavelength,  $\lambda_{\text{rf}} = \lambda / (1 + z_q)$  (for quasar redshift  $z_q$ ), multiplied by a mean transmission fraction that slowly varies with absorber redshift. Following this assumption, the universal spectrum is found by stacking the appropriately normalized spectra of quasars in our sample, thus averaging out the fluctuating Ly $\alpha$  absorption. The product  $C_q \bar{F}$  for individual quasars is then derived from the universal spectrum by normalizing it to account for the quasar’s mean forest flux and then modifying its slope to account for spectral-index diversity and/or photo-spectroscopic miscalibration.

Method 1 estimates directly the product  $C_q \bar{F}$  in equation 2. An example is given by the red line in figure 3. The estimate is made by modeling each spectrum as

$$C_q \bar{F} = a_q \left( \frac{\lambda}{\langle \lambda \rangle} \right)^{b_q} \bar{f}(\lambda_{\text{rf}}, z) \quad (6)$$

where  $a_q$  is a normalization,  $b_q$  a “deformation parameter”, and  $\langle \lambda \rangle$  is the mean wavelength in the forest for the quasar  $q$  and  $\bar{f}(\lambda_{\text{rf}}, z)$  is the mean normalized flux obtained by stacking spectra in bins of width  $\Delta z = 0.1$ :

$$\bar{f}(\lambda_{\text{rf}}, z) = \sum_q w_q f_q(\lambda) / f_q^{128} / \sum_q w_q. \quad (7)$$

Here  $z$  is the redshift of the absorption line at observed wavelength  $\lambda$  ( $z = \lambda / \lambda_{\text{Ly}\alpha} - 1$ ),  $f_q$  is the observed flux of quasar  $q$  at wavelength  $\lambda$  and  $f_q^{128}$  is the average of the flux of quasar  $q$  for  $127.5 < \lambda_{\text{rf}} < 128.5$  nm. The weight  $w_q(\lambda)$  is given by  $w_q^{-1} = 1 / [\text{ivar}(\lambda) \cdot (f_q^{128})^2] + \sigma_{\text{flux, LSS}}^2$ . The quantity  $\text{ivar}$  is the pipeline estimate of the inverse flux variance in the pixel corresponding to wavelength  $\lambda$ . The quantity  $\sigma_{\text{flux, LSS}}^2$  is the contribution to the variance in the flux due to the LSS. We approximate it by its value at the typical redshift of the survey,  $z \sim 2.3$ :  $\sigma_{\text{flux, LSS}}^2 \sim 0.035$  (section 3.3).

Figure 4 shows the resulting mean  $\delta_i$  as a function of observed wavelength. The mean fluctuates about zero with up to 2% deviations with correlated features that include the H and K lines of singly ionized calcium (presumably originating from some combination of solar neighborhood, interstellar medium and the Milky Way halo absorption) and features related to Balmer lines. These Balmer features are a by-product of imperfect masking of Balmer absorption lines in F-star spectroscopic standards, which are used to produce calibration vectors (in the conversion of CCD counts to flux) for DR9 quasars. Therefore such Balmer artifacts are constant for all fibers in a plate fed to one of the two spectrographs and so they are approximately constant for every ‘half-plate’.

If unsubtracted, the artifacts in figure 4 would lead to spurious correlations, especially between pairs of pixels with separations that are purely transverse to the line of sight. We have made a global correction by subtracting the quantity  $\langle \delta \rangle(\lambda)$  in figure 4 (un-smoothed) from individual measurements of  $\delta$ . This is justified if the variance of the artifacts from half-plate-to-half-plate is sufficiently small, as half-plate-wide deviations from our global correction could, in principle add spurious correlations.

We have investigated this variance both by measuring the Balmer artifacts in the calibration vectors themselves and by studying continuum regions of all available quasars in the DR9 sample. Both studies yield no detection of excess variance arising from these artifacts, but do provide upper limits. The study of the calibration vectors indicate that the square-root of the variance is less than 20% of the mean Balmer artifact deviations and the study of quasar spectra indicate that the square-root of the variance is less than 100% of the mean Balmer artifacts (and less than 50% of the mean calcium line deviations).

We then performed Monte Carlo simulations by adding a random sampling of our measured artifacts to our data to confirm that our global correction is adequate. We found that there is no significant effect on the determination of the BAO peak position, even if the variations are as large as that allowed in our tests.

### 3.2. Continuum fits, method 2

Method 1 would be especially appropriate if the fluxes had a Gaussian distribution about the mean absorbed flux,  $C_q \bar{F}$ . Since this is not the case, we have developed method 2 which explicitly uses the probability distribution function for the transmitted flux fraction  $F$ ,  $P(F, z)$ , where  $0 < F < 1$ . We use the  $P(F, z)$  that results from the log-normal model used to generate mock data (see appendix A).

Using  $P(F, z)$ , we can construct for each BOSS quasar the PDF of the flux in pixel  $i$ ,  $f_i$ , by assuming a continuum  $C_q(\lambda_i)$  and convolving with the pixel noise,  $\sigma_i$ :

$$P_i(f_i, C_q(\lambda_i), z_i) \propto \int_0^1 dF P(F, z_i) \exp \left[ \frac{-(C_q F - f_i)^2}{2\sigma_i^2} \right]. \quad (8)$$

The continuum is assumed to be of the form

$$C_q(\lambda) = (a_q + b_q \lambda) \bar{f}(\lambda_{\text{rf}}) \quad (9)$$

where  $\bar{f}(\lambda_{\text{rf}})$  is the mean flux as determined by stacking spectra as follows:

$$\bar{f}(\lambda_{\text{rf}}) = \sum_q w_q(\lambda_{\text{rf}}) [f_q(\lambda_{\text{rf}}) / f_q^{128}] / \sum_q w_q \quad (10)$$

as in equation 7 except that here there is no redshift binning. The parameters  $a_q$  and  $b_q$  are then determined for each quasar by maximizing a likelihood given by

$$L(C_q) = \prod_i P_i[f_i, C_q(\lambda_i)]. \quad (11)$$

Figure 3 shows the  $C_q(\lambda)$  estimated for a typical quasar (blue line).

The last element necessary to use equation (2) is the mean transmitted flux fraction  $\bar{F}(z)$ . If  $P(F, z)$  derived from the mocks were the true distribution of the transmitted flux fraction, then  $\bar{F}(z)$  could simply be computed from the average of this distribution. Since this is not precisely true, we determine  $\bar{F}(z)$  from the data by requiring that the mean of the delta field vanish for all redshifts. The  $\bar{F}(z)$  we obtain is shown in figure 5. The unphysical wiggles in the derived  $\bar{F}(z)$  are associated with the aforementioned residuals in  $\delta(\lambda)$  for method 1 (figure 4).

There is one inevitable effect of our two continuum estimating procedures. The use of the forest data in fitting the continuum effectively forces each quasar to have a mean absorption near that of the mean for the entire quasar sample. This approach introduces a spurious negative correlation between pixels on a given quasar even when well separated in wavelength. This negative correlation has no direct effect on our measurement of the flux correlation function because we do not use pixel pairs from the same quasar. However, the physical correlation between absorption on neighboring quasars causes the unphysical negative correlation for individual quasars to generate a negative contribution to the correlation measured with quasar pairs. Fortunately, this distortion is a smooth function of scale so it can be expected to have little effect on the observability or position of the BAO peak. This expectation is confirmed by analysis of the mock spectra (section 5).

### 3.3. Weights

A discussion on the optimal use of weights for the Ly $\alpha$  correlation function is found in McQuinn & White (2011). Here we

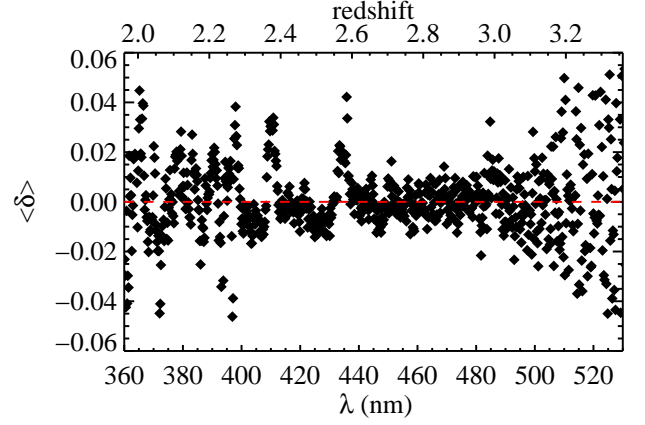


**Fig. 4.** The mean of  $\delta(\lambda)$  plotted as a function of observed wavelength (method 1). Systematic offsets from zero are seen at the 2% level. The calcium lines (393.4, 396.8 nm) is present. The features around the hydrogen lines H $\gamma$ ,  $\delta$  and  $\epsilon$  (434.1, 410.2, 397.0 nm) are artifacts from the use of F-stars for the photocalibration of the spectrometer.

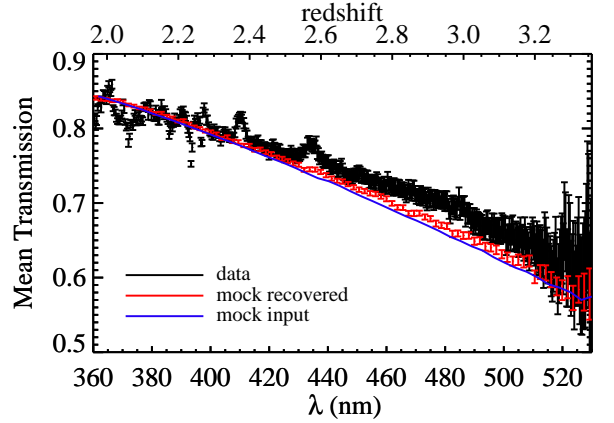


**Fig. 5.** Mean transmitted flux fraction as a function of redshift obtained from the continuum fits with method 2. Data are shown in black, mock-000 in red and the input mean transmitted flux fraction in blue.

simply choose the weights  $w_{ij}$  so as to approximately minimize the relative error on  $\hat{\xi}_A$  estimated with equation (3). In the approximation of uncorrelated pixels, the variance of  $\hat{\xi}_A$  is

$$\text{Var}(\hat{\xi}_A) = \frac{\sum_{i,j \in A} w_{ij}^2 \xi_{ii} \xi_{jj}}{\left[ \sum_{i,j \in A} w_{ij} \right]^2} \quad \xi_{ii} = \langle \delta_i^2 \rangle \quad (12)$$

where the pixel variance,  $\xi_{ii}$ , includes contributions from both observational noise and LSS. The signal-to-noise ratio is:

$$\left( \frac{S}{N} \right)^2 = \frac{\langle \hat{\xi}_A \rangle^2}{\text{Var}(\hat{\xi}_A)} \simeq \frac{\left( \sum_{i,j \in A} \xi_{ij} w_{ij} \right)^2}{\sum_{i,j \in A} \xi_{ii} \xi_{jj} w_{ij}^2}. \quad (13)$$

Because of LSS growth and redshift evolution of the mean absorption, the  $\xi_{ij}$  depend on redshift and we use the measured dependence of the 1d correlation function (McDonald et al., 2006)

$$\xi_{ij}(z) = (1 + z_i)^{\gamma/2} (1 + z_j)^{\gamma/2} \xi_{ij}(z_0) \quad \gamma \sim 3.8. \quad (14)$$



Maximizing the signal-to-noise ratio with respect to  $w_{ij}$  this gives:

$$w_{ij} \propto \frac{(1+z_i)^{\gamma/2}(1+z_j)^{\gamma/2}}{\xi_{ii}^2 \xi_{jj}^2}. \quad (15)$$

For this expression to be used, we require a way of estimating the  $\xi_{ii}$ . We assume that it can be decomposed into a noise term and a LSS term ( $\sigma_{\text{LSS}}$ ):

$$\xi_{ii}^2 = \frac{\sigma_{\text{pipeline},i}^2}{\eta(z_i)} + \sigma_{\text{LSS}}^2(z_i) \quad z_i = \lambda_i/\lambda_{\text{Ly}\alpha} - 1, \quad (16)$$

where  $\sigma_{\text{pipeline},i}^2 = [\text{ivar}(C_q \bar{F})^2]^{-1}$  is the pipeline estimate of the noise-variance of pixel  $i$  and  $\eta$  is a factor that corrects for a possible misestimate of the variance by the pipeline.

We then organize the data in bins of  $\sigma_{\text{pipeline},i}^2$  and redshift. In each such bin, we measure the variance of  $\delta_i$ , which serves as an estimator of  $\xi_{ii}$  for the bin in question. The two functions  $\eta(z)$  and  $\sigma_{\text{LSS}}^2(z)$  can then be determined by fitting equation (16).

These fits are shown in figure 6. The top panel shows that the measured inverse variance follows the inverse pipeline variance until saturating at the redshift-dependent LSS variance (shown on the bottom left panel). For  $z > 3$ , there are not enough pixel pairs to determine  $\eta(z)$  and  $\sigma_{\text{LSS}}^2(z)$ . In this high redshift range, we assumed  $\eta = 1$  and extrapolated  $\sigma_{\text{LSS}}^2(z)$  with a second-degree polynomial fit to the  $z < 3$  data.

### 3.4. $\xi(r, \mu)$

The procedure described above was used to determine  $\xi(r, \mu)$  through equation 3 in  $r$ -bins of width  $4 \text{ h}^{-1}\text{Mpc}$  (centered at 2.6, ..., 198  $\text{h}^{-1}\text{Mpc}$ ) and in  $\mu$ -bins of width 0.02, (centered at 0.01, 0.03, ... 0.99). The  $50 \times 50 \text{ } r-\mu$  bins have an average of  $6 \times 10^6$  terms in the sum (3) with an average nominal variance of  $\xi$  for individual bins of  $(10^{-4})^2$  as given by (eqn.12).

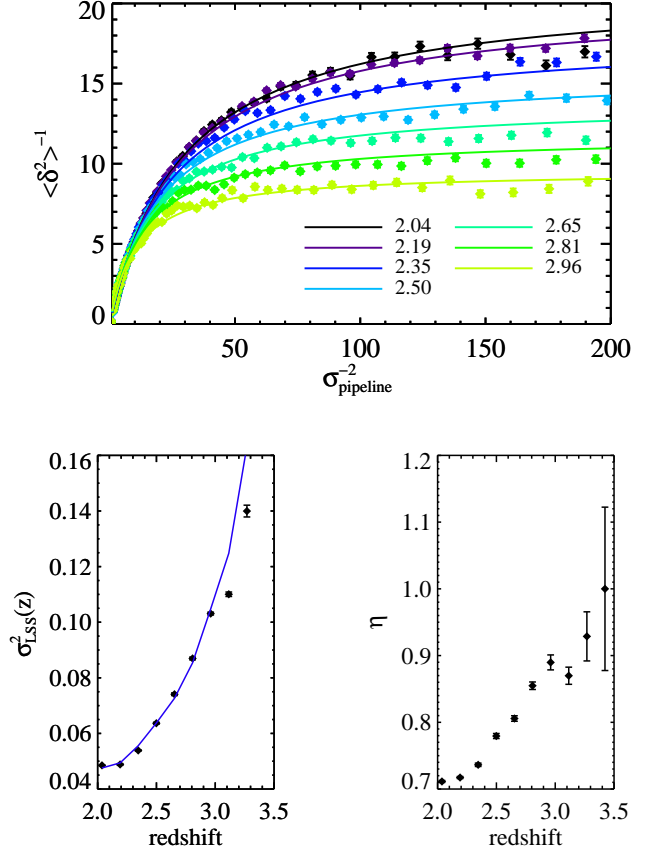
Figure 7 shows an example of  $\xi(r, \mu)$  for the  $r$  bin centered on 34  $\text{h}^{-1}\text{Mpc}$ . The blue dots are the data and the red dots are the mean of the 15 mocks. The function falls from positive to negative values with increasing  $\mu$ , as expected from redshift distortions. The effect is enhanced by the deformation due to the continuum subtraction.

Figure 8 presents  $\xi(r, \mu)$  averaged over three bins in  $\mu$ . A clear peak at the expected BAO position,  $r_s = 105 \text{ h}^{-1}\text{Mpc}$ , is present in the bin  $0.8 < \mu < 1.0$  corresponding to separation vectors within  $37^\circ$  of the line-of-sight. The curves show the best fits for a  $\Lambda\text{CDM}$  correlation function, as described in section 5.

The data were divided into various subsamples to search for systematic errors in  $\xi(r, \mu)$ . For example, searches were made for differences between the northern and southern Galactic cap regions and between higher and lower signal-to-noise ratio quasars. No significant differences were found in the overall shape and amplitude of the correlation function. We also verified that the BAO peak position does not change significantly when wavelength slices of Ly $\alpha$  forest data are eliminated, in particular slices centered on the Balmer features in figure 4. The peak position also does not change significantly if the subtraction of the mean  $\delta$  (figure 4) is suppressed.

## 4. The Monopole and quadrupole

The analysis of the correlation function was performed in the framework of the standard multipole decomposition (Hamilton,



**Fig. 6.** Top panel: Inverse total variance in bins of redshift as a function of the pipeline inverse variance. Bottom panel: Parameters of the fit: the LSS contribution  $\sigma_{\text{LSS}}^2$  (left) and the pipeline correction factor  $\eta$  (right) as a function of redshift. The lines show fits to the data as explained in the text.

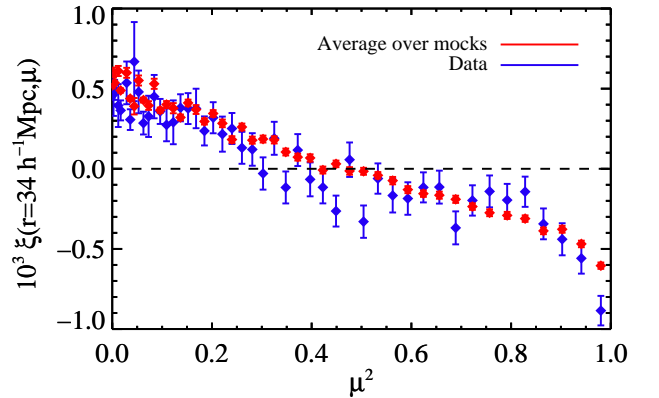


**Fig. 7.**  $\xi(r, \mu)$  vs.  $\mu^2$  for the bin centered on  $r = 34 \text{ h}^{-1}\text{Mpc}$ . The red dots are the mean of the 15 mocks and the blue dots are the data.

1992). For each bin in  $r$  we fit a monopole ( $\ell = 0$ ) and quadrupole ( $\ell = 2$ ) to the angular dependence:

$$\hat{\xi}(r, \mu) = \sum_{\ell=0,2} \xi_{\ell}(r) P_{\ell}(\mu) = [\xi_0(r) - \xi_2(r)/2] + [3\xi_2(r)/2]\mu^2 \quad (17)$$

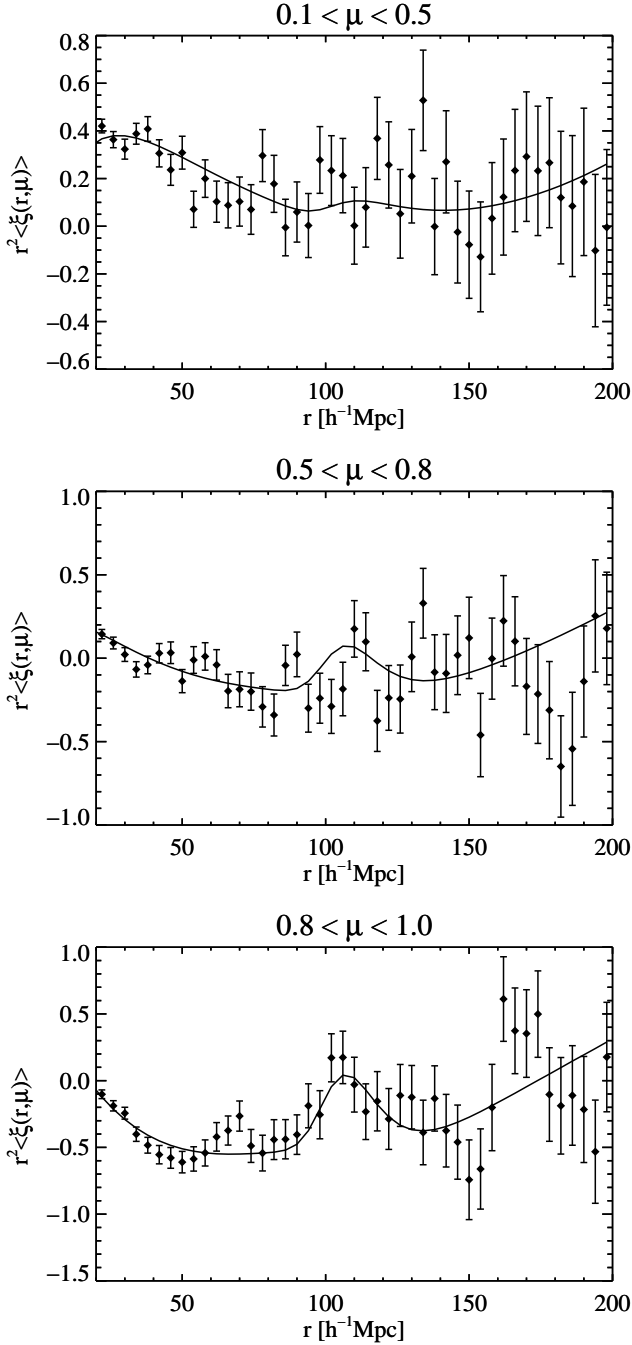


**Fig. 8.**  $\xi(r, \mu)$  averaged over  $0.1 < \mu < 0.5$ ,  $0.5 < \mu < 0.8$  and  $0.8 < \mu < 1$ . The curves give fits (section 5) to the data imposing concordance  $\Lambda$ CDM cosmology. The BAO peak is most clearly present in the data for  $\mu > 0.8$ .

where  $P_\ell$  is the  $\ell$ -Legendre polynomial. We ignore the small and poorly determined  $\ell = 4$  term. This fit is performed using a simple  $\chi^2$  minimization with the nominal variance (equation 12) and ignoring the correlations between bins. This approach makes the fit slightly sub-optimal. (Later, we will correctly take into account correlations between  $r$ -bins of the monopole and quadrupole.) We also exclude from this fit the portion  $\mu < 0.1$  to avoid residual biases due to correlated sky subtraction across quasars; this has a negligible impact on the fits and, at any rate, there is little BAO signal at low  $\mu$ .

Figure 9 displays the monopole and quadrupole signals found by the two methods. The two methods are slightly offset from one another, but the peak structure is very similar. Figure 9 also shows the combination  $\xi_0 + 0.1\xi_2$  which, because of the small monopole-quadrupole anti-correlation (section 4.1), is a better-determined quantity. The peak structure seen in figure 8 is also present in these figures.

Because of the continuum estimation procedure (sections 3.1 and 3.2), we can expect that the monopole and quadrupole shown in figure 9 are deformed with respect to the true monopole and quadrupole. The most important difference is that the measured monopole is negative for  $60 \text{ h}^{-1}\text{Mpc} < r < 100 \text{ h}^{-1}\text{Mpc}$  while the true  $\Lambda$ CDM monopole remains positive for all  $r < 130 \text{ h}^{-1}\text{Mpc}$ . The origin of the deformation in the continuum estimate is demonstrated in appendix A where both the true and estimated continuum can be used to derive the correlation function (figure A.1). As expected, the deformation is a slowly varying function of  $r$  so neither the position of the BAO peak nor its amplitude above the slowly varying part of the correlation function are significantly affected.

#### 4.1. Covariance of the monopole and quadrupole

In order to determine the significance of the peak we must estimate the covariance matrix of the monopole and quadrupole. If the fluctuations  $\delta_i$  in equation (3) in different pixels were uncorrelated, the variance of  $\xi_A$  would simply be the weighted products of the fluctuation variances. This yields a result that is  $\sim 30\%$  smaller than the true correlation variance that we compute below. The reason is, of course, that the  $\delta$ -pairs are correlated, either from LSS or from correlations induced by instrumental effects or continuum subtraction; this effect reduces the effective number of pairs and introduces correlations between  $(r, \mu)$  bins.

Rather than determine the full covariance matrix for  $\xi(r, \mu)$ , we determined directly the covariance matrix for  $\xi_0(r)$  and  $\xi_2(r)$  by standard techniques of dividing the full quasar sample into subsamples according to position on the sky. In particular we used the sub-sampling technique described below. We also tried a bootstrap technique (e.g. Efron & Gong, 1983) consisting of substituting the entire set of  $N$  subdivisions of the data by  $N$  of these subdivisions chosen at random (with replacement) to obtain a “bootstrap” sample. The covariances are then measured from the ensemble of bootstrap samples. Both techniques give consistent results.

The adopted covariance matrix for the monopole and quadrupole uses the sub-sampling technique. We divide the data into angular sectors and calculate a correlation function in each sector. Pairs of pixels belonging to different sectors contribute only to the sector of the pixel with lower right ascension. We investigated two different divisions of the sky data: defining 800 (contiguous but disjoint) sectors of similar solid angle, and taking the plates as defining the sectors (this latter version does not lead to disjoint sectors). The two ways of dividing the data lead to similar covariance matrices.

Each sector  $s$  in each division of the data provides a measurement of  $\xi_s(r, \mu)$  that can be used to derive a monopole and quadrupole,  $\xi_{\ell s}(r)$ , ( $\ell = 0, 2$ ). The covariance of the whole BOSS sample can then be estimated from the weighted and rescaled covariances for each sector:

$$\begin{aligned} & \sqrt{W(r)W(r')} \text{Cov}[\hat{\xi}_\ell(r), \hat{\xi}_{\ell'}(r')] \\ &= \left\langle \sqrt{W_s(r)W_{s'}(r')} \left[ \hat{\xi}_{\ell s}(r) \hat{\xi}_{\ell' s'}(r') - \bar{\xi}_\ell(r) \bar{\xi}_{\ell'}(r') \right] \right\rangle. \end{aligned} \quad (18)$$



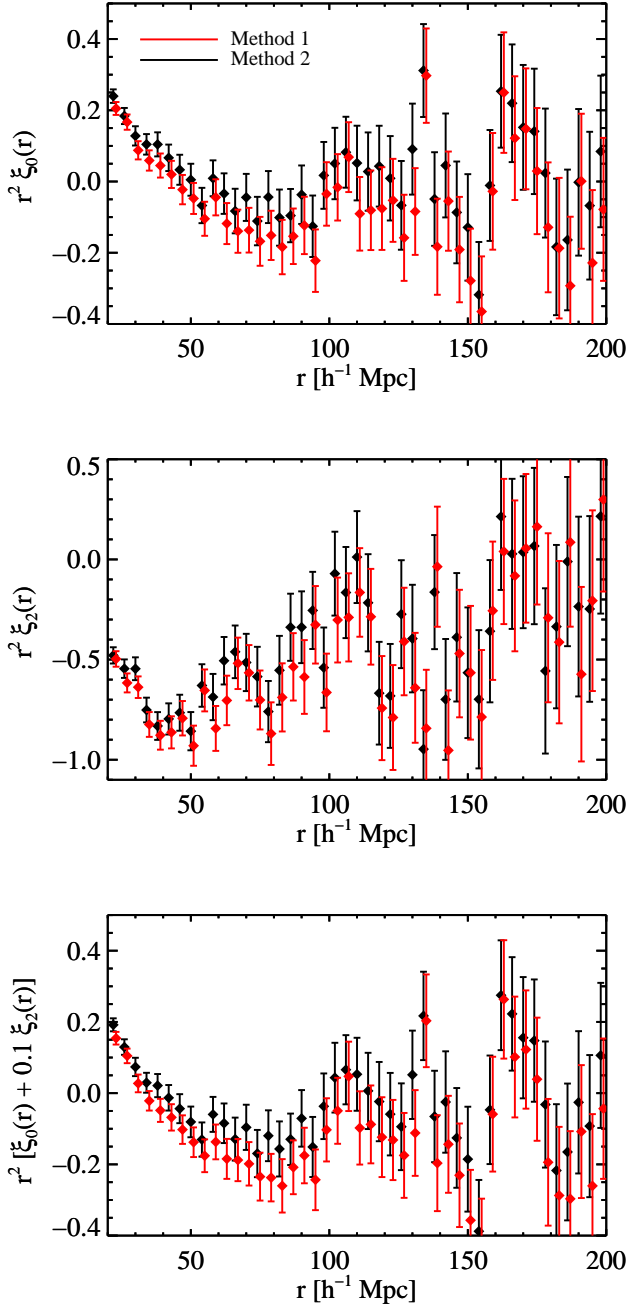


**Fig. 9.** Monopole (upper panel) and quadrupole (middle panel) correlation functions found by method 1 (red) and method 2 (black). The bottom panel shows the combination  $\xi_0 + 0.1\xi_2$  found by method 1 (red) and method 2 (black).

The average denoted by  $\langle \rangle$  is the simple average over sectors, while  $\tilde{\xi}_r(r)$  denotes the correlation function measured for the whole BOSS sample. The  $W_s(r)$  are the summed pixel-pair weights for the radial bin  $r$  for the sector  $s$  and  $W(r)$  is the same sum for the whole BOSS sample.

The most important terms in the covariance matrix are the  $r = r'$  terms, i.e. the monopole and quadrupole variances. They are shown in figure 10 as a function of  $r$ . In the figure, they are multiplied by the number  $N$  of pixel pairs in the  $r$ -bin. The product is nearly independent of  $r$ , as expected for a variance nearly equal to the pixel variance divided by  $N$ . For the monopole, the

variances are only about 30% higher than what one would calculate naively assuming uncorrelated pixels and equation (12). Figure 10 also displays the monopole-quadrupole covariance times number of pairs, which also is nearly independent of  $r$ .

Figure 11 displays the monopole-monopole and quadrupole-quadrupole covariances. Nearest-neighbor covariances are of order 20%. Figure 11 also shows monopole-quadrupole covariance.

We used the 15 sets of mock spectra to test our method for calculating the covariance matrix. From the 15 measurements of  $\xi_\ell(r)$  one can calculate the average values of  $\xi_\ell(r)\xi_{\ell'}(r')$  and compare them with those expected from the covariance matrix. Figures 12 shows this comparison for the monopole and quadrupole variance, the monopole and quadrupole covariances between neighboring  $r$ -bins and the monopole-quadrupole covariance. The agreement is satisfactory.

#### 4.2. Detection significance of the BAO peak

In this section, we estimate the significance of our detection of a BAO peak at  $105 \text{ h}^{-1} \text{ Mpc}$ . At the statistical power of the present data, it is clear that the peak significance will depend to some extent on how we treat the so-called “broadband” correlation function on which the peak is superimposed. In particular, the significance will depend strongly on the  $r$ -range over which the correlation functions are fitted. To the extent that the BAO peak is known to be present in the matter correlation function and that the Ly $\alpha$  absorption is known to trace matter, the actual significance is of limited interest for cosmology. Of greater interest is the uncertainty in the derived cosmological parameter constraints (section 5) which will be non-linear reflections of the peak significance derived here.

A detection of the BAO peak requires comparing the quality of a fit with no peak (the null hypothesis) to that of a fit with a peak. Typically, this exercise would be performed by choosing a test statistic, such as the  $\chi^2$ , computing the distribution of this quality indicator from a large number of peak-less simulations and looking at the consistency of the data with this distribution. Since our mock data sets are quite computationally expensive and only a handful are available, we chose a different approach.

Our detection approach uses the following expression to fit the observed monopole and quadrupole.

$$\xi_\ell(r) = B_\ell \xi_\ell^{BB}(r) + C_\ell \xi_\ell^{\text{peak}}(r) + A_\ell \xi_\ell^{\text{dist}}(r) \quad (19)$$

where  $\xi_\ell^{BB}$  is a broadband term to describe the LSS correlation function in the absence of a peak,  $\xi_\ell^{\text{peak}}$  is a peak term, and  $\xi_\ell^{\text{dist}}$  is a “distortion” term used to model the effects of continuum subtraction. The broadband term is derived from the fiducial  $\Lambda\text{CDM}$  cosmology defined by the parameters in equation (A.1). It is obtained by fitting the shape of the fiducial correlation function with an 8-node spline function *masking the region of the peak* ( $80 \text{ h}^{-1} \text{ Mpc} < r < 120 \text{ h}^{-1} \text{ Mpc}$ ). The peak term is the difference between the theoretical correlation function and the broadband term. Finally, the distortion term is calculated from simulations, as the difference in the monopole or quadrupole measured using the true continuum and that measured from fitting the continuum as described in appendix A. The three components are shown in figure 13.

Expression (19) contains three parameters each for the monopole and quadrupole (so six in total). We have performed fits leaving all six parameters free and fits where we fix the ratio  $C_2/C_0$  to be equal to its nominal value used to generate our

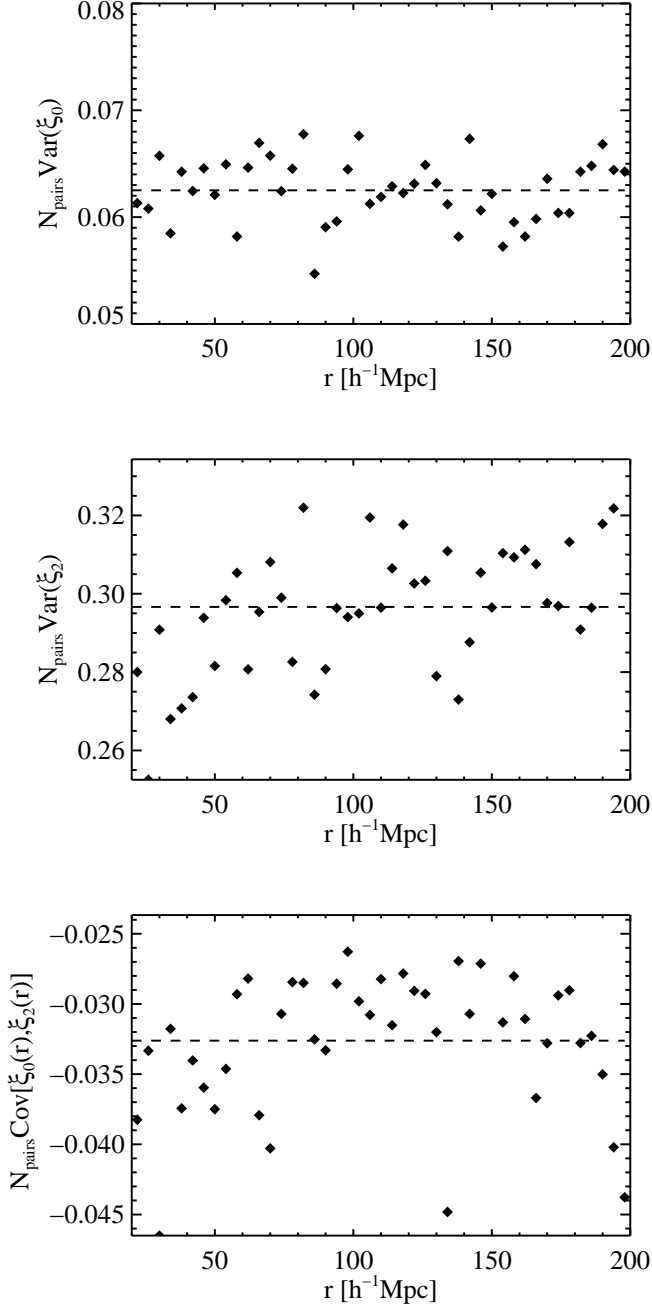


**Fig. 10.** The  $r$ -dependence of the product of the monopole (top) and quadrupole (middle) variances and the number of pairs in the  $r$ -bin. The bottom panel shows the product for the monopole-quadrupole covariance ( $r = r'$  elements). The dotted lines show the means for  $r > 20 h^{-1}\text{Mpc}$ .

mock spectra (the value given by assuming a “redshift distortion parameter”  $\beta = 1.4$ , see appendix A). We define the test statistic as the  $\chi^2$  difference between fitting equation (19) simultaneously to monopole and quadrupole by fixing  $C_0$  to zero (a “peak-less” four or five-parameter fit) and fitting for  $C_0$  (a five or six-parameter fit). In our detection fits we do not fit for the BAO position but fix it to the theoretical prediction. The distribution for this test statistic (“ $\Delta\chi^2_{\text{det}}$ ”) under the null hypothesis is a  $\chi^2$  distribution with one degree of freedom. The significance is then given by  $\sigma = (\Delta\chi^2_{\text{det}})^{1/2}$ .

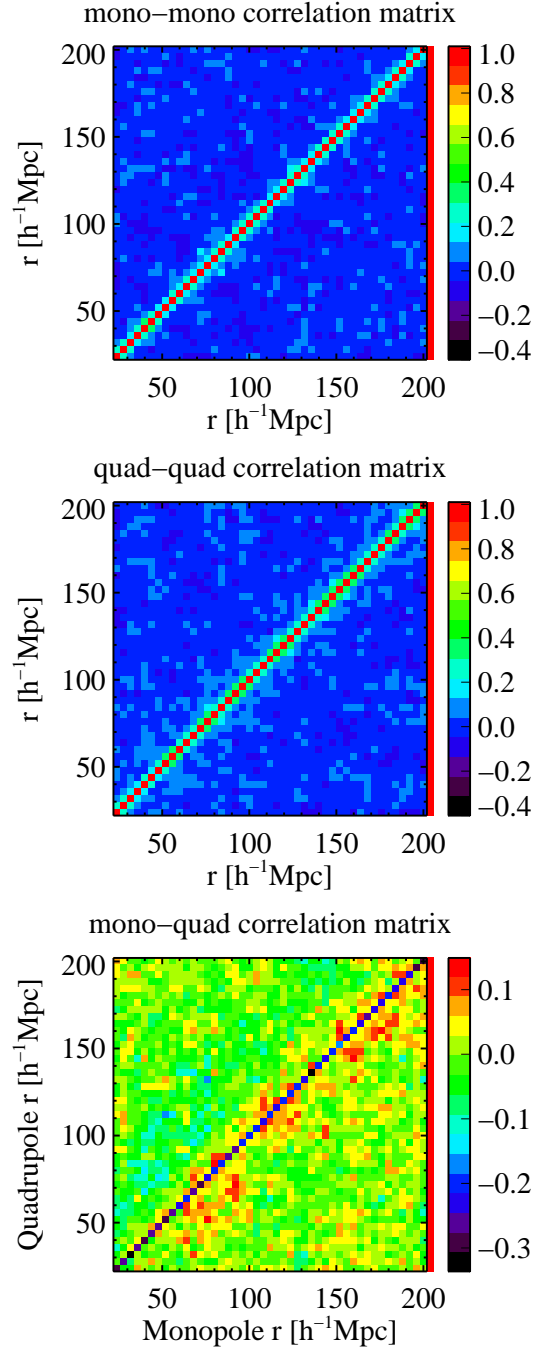


**Fig. 11.** The monopole and quadrupole covariance matrix. The monopole-monopole and quadrupole-quadrupole elements are normalized to the variance:  $C_{ij}/\sqrt{C_{ii}C_{jj}}$ . The monopole-quadrupole elements are normalized to the mean of the quadrupole and monopole variances. The first off-diagonal elements of the monopole-monopole and quadrupole-quadrupole elements are  $\sim 20\%$  of the diagonal elements. The diagonal elements of the quadrupole-monopole covariance are  $\sim -0.2$  times the geometric mean of the monopole and quadrupole variances.

Figure 14 shows the fits to monopole (top panel) and quadrupole (bottom panel) and the corresponding fits with and without peaks and fixing  $\beta = 1.4$ . For method 2, we obtain  $\chi^2/\text{DOF} = 93.7/85$  (111.8/86) with (without) a peak, giving  $\Delta\chi^2 = 18.1$  for a detection significance of  $4.2\sigma$ . For method 1, we obtain  $\chi^2/\text{DOF} = 93.2/85$  (102.2/86) for a significance

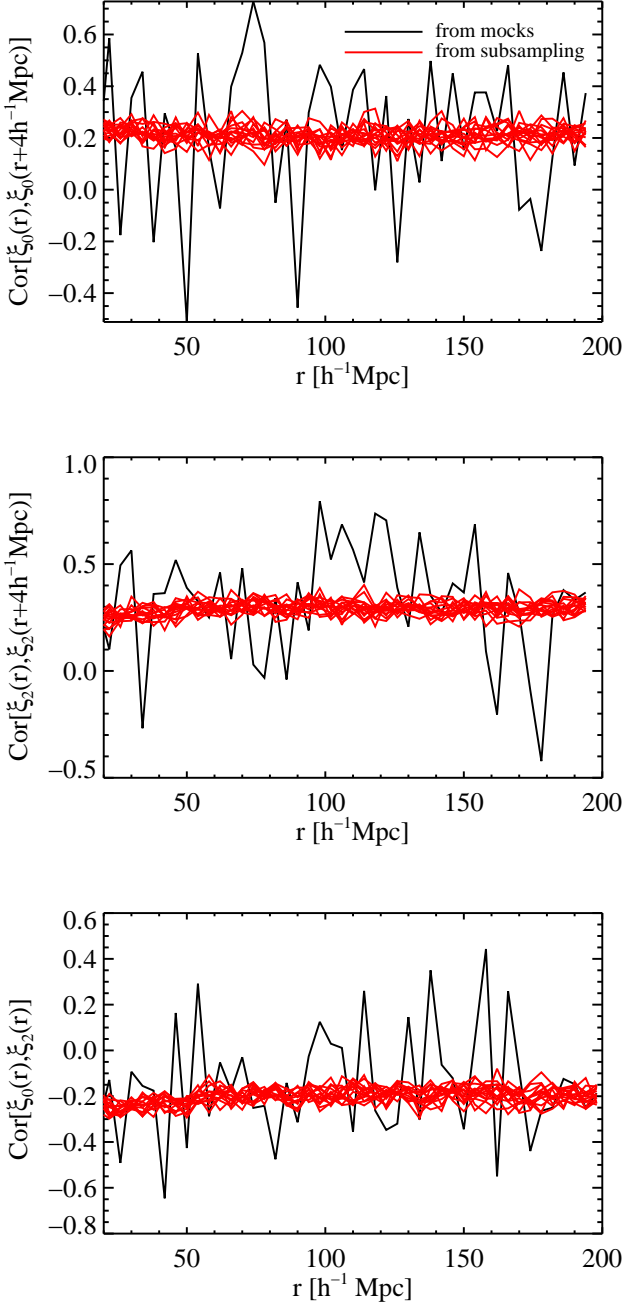


**Fig. 12.** Verification of the off-diagonal elements of the covariance matrix with the 15 sets of mock spectra. The black lines show correlations derived from the dispersion of the 15 measurements and the red lines show the correlations expected from the covariance matrix calculated by sub-sampling. The top and middle panels show the correlation between neighboring bins for monopole and quadrupole respectively. The bottom panel the correlation between monopole and quadrupole measured at the same distance bin.

of  $3.0\sigma$ . Allowing  $\beta$  to be a free parameter gives essentially the same detection significances.

The detection significance of  $\sim 4\sigma$  is typical of that which we found in the 15 sets of mock spectra. For the mocks, the significances ranged from 0 to  $6\sigma$  with a mean of  $3.5\sigma$ .

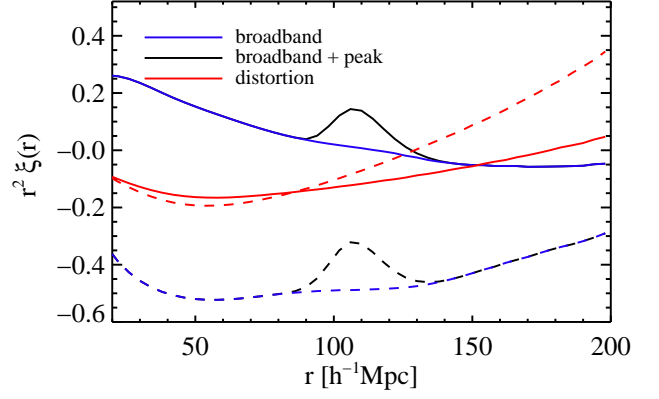


**Fig. 13.** The fitting functions used for the determination of the peak detection significance:  $r^2\xi^{bb}(r)$  (blue),  $r^2[\xi^{peak}(r) + \xi^{bb}(r)]$  (black) and  $r^2\xi^{dist}(r)$  (red) for the monopole (solid lines) and quadrupole (dashed lines).

Our significance depends strongly on the fitting range. For a lower boundary of the range of  $r_{\min} = 20, 40, 60 \text{ h}^{-1}\text{Mpc}$  we obtain a significance of  $\sigma = 4.2, 3.2$  and  $2.3$ , respectively (method 2). The reason for this result is illustrated in figure 15, where the results of the fits with and without peaks are compared to data for different values of  $r_{\min} = 20, 40, 60 \text{ h}^{-1}\text{Mpc}$ . Reducing the fitting range poses less stringent constraints on the distortion and broadband terms, thus allowing some of the peak to be attributed to the broadband. In particular, the statistically insignificant bump in the quadrupole at  $\sim 65 \text{ h}^{-1}\text{Mpc}$  causes the fitted broadband to increase as  $r_{\min}$  is increased to  $60 \text{ h}^{-1}\text{Mpc}$ , decreasing the amplitude of the BAO peak. For the monopole, the  $r_{\min} = 60 \text{ h}^{-1}\text{Mpc}$  fit predicts a positive slope for  $\xi_0(r)$  that decreases the amplitude of the peak but predicts a  $\xi_0(r < 50 \text{ h}^{-1}\text{Mpc})$  to be much less than what is measured.

## 5. Cosmology with the BAO peak

The observed position of the BAO peak in  $\xi(r, \mu)$  is determined by two sets of cosmological parameters: the “true” parameters and the “fiducial” parameters. Nature uses the true cosmology to create correlations at the true sound horizon,  $r_s$ . The true cosmology transforms physical separations between Ly $\alpha$  absorbers into angles on the sky and redshift differences:  $\theta_{BAO} = r_s/D_A(z)(1+z)$  and  $\Delta z_{BAO} = r_s H(z)/c$ . We, on the other hand, use a “fiducial” cosmology (defined by equation A.1) to transform angular and redshift differences to local distances at the redshift in question to reconstruct  $\xi(r, \mu)$ . If the fiducial cosmology is the true cosmology, the reconstructed peaks will be at the calculated fiducial sound horizon,  $r_{s,f}$ . Limits on the difference between the fiducial and reconstructed peak position can be used to constrain the differences between the fiducial and true cosmological models.

### 5.1. The peak position

The use of incorrect fiducial  $D_A$ ,  $H$  and  $r_s$  leads to shifts in the BAO peak position in the transverse and radial directions by the multiplicative factors  $\alpha_t$  and  $\alpha_r$ :

$$\alpha_t \equiv \frac{D_A(z)/r_s}{D_{A,f}/r_{s,f}} \quad (20)$$

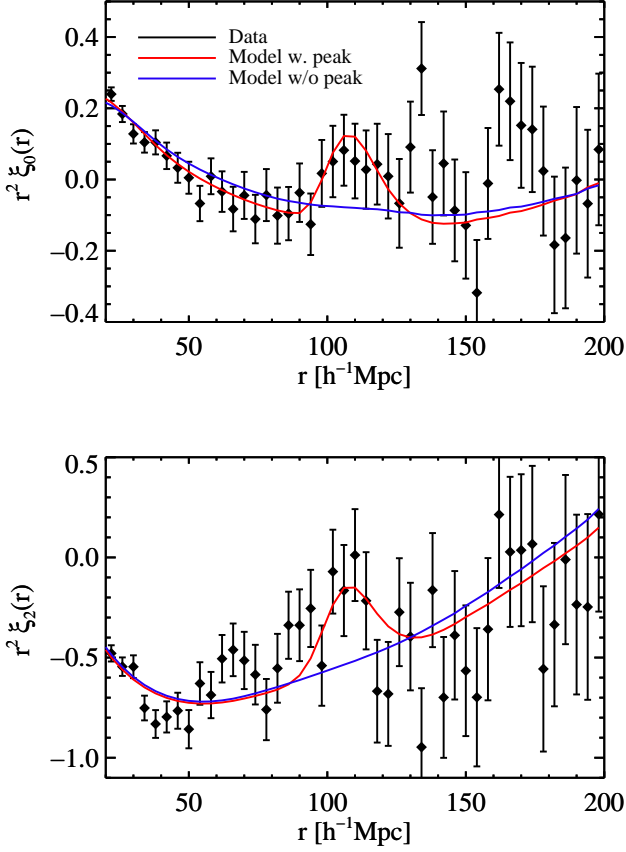


**Fig. 14.** Monopole and quadrupole fits with a BAO peak (red line) and without a BAO peak (blue line, Method 2). The fitting range is  $r_{\min} < r < 200 \text{ h}^{-1}\text{Mpc}$  with  $r_{\min} = 20 \text{ h}^{-1}\text{Mpc}$ .

$$\alpha_r \equiv \frac{H_f(z)r_{s,f}}{H(z)r_s} \quad (21)$$

where the subscript  $f$  refers to the fiducial model. Following Xu et al. (2012), we will use a fitting function,  $\tilde{\xi}_\ell(r)$ , for the monopole and quadrupole that follows the expected peak position as a function of  $(\alpha_t, \alpha_r)$ :

$$\tilde{\xi}_\ell(r) = \hat{\xi}_\ell(r, \alpha_t, \alpha_r, b, \beta) + A_\ell(r) \quad \ell = 0, 2. \quad (22)$$

Here, the two functions  $\hat{\xi}_\ell$ , derived from the power spectrum given in appendix A, describe the underlying mass correlation function, the linear bias  $b$  and redshift distortion parameter  $\beta$ , and the movement of the BAO peak for  $\alpha_t, \alpha_r \neq 1$ . The functions  $A_\ell$  take into account distortions, as described below.

For  $\alpha_t = \alpha_r \equiv \alpha_{iso}$ , there is a simple isotropic scaling of the coordinates by  $\alpha_{iso}$  and  $\hat{\xi}_\ell(r)$  is given by  $\hat{\xi}_\ell(r, \alpha_{iso}) = f_\ell(b, \beta) \xi_{\ell,f}(\alpha_{iso} r)$ , where  $\xi_{\ell,f}$  are the fiducial monopole and quadrupole and the normalizations  $f_\ell$  are the functions of the bias and redshift-distortion parameter given by Hamilton (1992). For  $\alpha_t \neq \alpha_r$ , Xu et al. (2012) found an approximate formula for  $\hat{\xi}_\ell(r)$  that was good in the limit  $|\alpha_t - \alpha_r| \ll 1$ . We take the more direct route of numerically expanding  $\xi_f(\alpha_t r_t, \alpha_r r_r)$  in Legendre polynomials,  $P_\ell(\mu)$ , to directly calculate the  $\hat{\xi}_\ell(r, \alpha_t, \alpha_r)$ .

The functions  $A_\ell(r)$  describe broadband distortions due to continuum subtraction and the fact that the broadband correlation function is not expected to change in the same way as the BAO peak position when one deviates from the fiducial model.

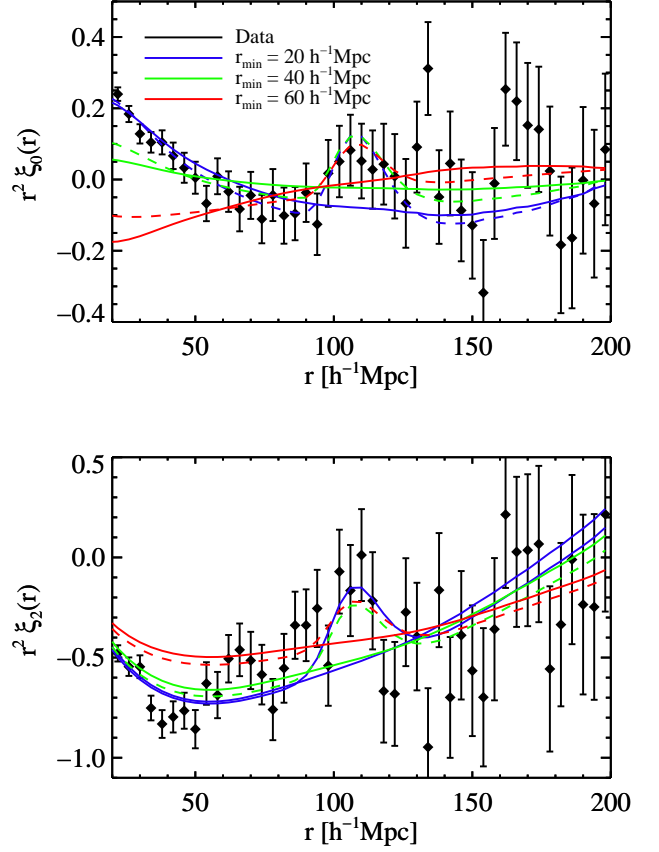


**Fig. 15.** Same as figure 14 except for different fitting ranges: blue, green and red curves are for fits with  $r_{\min} = 20 \text{ h}^{-1}\text{Mpc}$ ,  $40 \text{ h}^{-1}\text{Mpc}$  and  $60 \text{ h}^{-1}\text{Mpc}$  respectively (Method 2). The solid lines for fits without a BAO peak and the dashed lines with a peak.

They correspond to the term  $A_\ell \xi_\ell^{\text{dist}}$  in equation (19). We have used two forms to represent  $A_\ell(r)$ :

$$A_\ell^{(1)}(r) = \frac{a_\ell}{r^2} + \frac{b_\ell}{r} + c_\ell \quad (23)$$

and

$$A_\ell^{(2)}(r) = \frac{a_\ell}{r^2} + \frac{b_\ell}{r} + c_\ell + \frac{d_\ell}{\sqrt{r}}. \quad (24)$$

The observed monopole and quadrupole can then be fit to (22) with free parameters  $\alpha_t, \alpha_r$ , bias,  $\beta$ , and the nuisance parameters ( $a_\ell, b_\ell, c_\ell$  and  $d_\ell$ ).

We first fixed  $(\alpha_t, \alpha_r) = (1, 1)$  to determine if we find reasonable values of  $(b, \beta)$ . These two parameters are highly degenerate since both the quadrupole and monopole have amplitudes that are proportional to  $b^2$  times polynomials in  $\beta$ . A well-determined combination is  $b(1 + \beta)$ , for which we find a value  $0.38 \pm 0.07$ ; this is in agreement with  $b(1 + \beta) = 0.336 \pm 0.012$  found at  $r \sim 40 \text{ h}^{-1}\text{Mpc}$  by Slosar et al. (2011). The larger error of our fit reflects the substantial freedom we have introduced with our distortion function.

We next freed all parameters to constrain  $(\alpha_t, \alpha_r)$ . The contours for the two methods and two broadband are shown in figure 16 and the  $\chi^2$  for the fiducial and best-fit models are given in table 1. The broadband term in equation (24) fits the data better

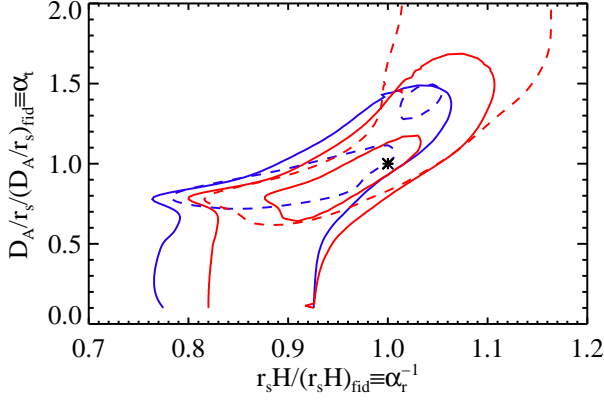


**Fig. 16.** The contours for  $(D_A/r_s, r_s H)$  obtained by fitting the monopole and quadrupole to (22). The broadband distortions are eqn. (23, dashed lines) or (24, solid lines). The blue lines are for method 1 and the red lines for method 2. All contours are for  $\Delta\chi^2 = 4$  except for the interior solid red contour which is for  $\Delta\chi^2 = 1$ .

than that in equation (23) both for the fiducial parameters and for the best fit. For broadband in equation (24), the  $\chi^2$  for the fiducial model is acceptable for both methods:  $\chi^2/DOF = 85.0/80$  for method 1 and  $\chi^2/DOF = 71.5/80$  for method 2.

The contours in the figure are elongated along the direction for which the BAO peak position stays approximately fixed at large  $\mu$  (near the radial direction, where the observations are most sensitive). The best constrained combination of  $D_A$  and  $H$  of the form  $(D_A^\zeta H^{\zeta-1}/r_s)$  turns out to have  $\zeta \sim 0.2$ . This low value of  $\zeta$  reflects the fact that we are mostly sensitive to the BAO peak in the radial direction. At the one standard-deviation level, the precision on this combination is about 4%. However, even this combination is sensitive to the tails in the contours. A more robust indicator of the statistical accuracy of the peak-position determination comes from fits imposing  $\alpha_l = \alpha_r \equiv \alpha_{iso}$ , as has generally been done in previous BAO studies with the exception of Chuang & Wang (2012) and Xu et al. (2012). This constraint does not correspond to any particular class of cosmological models. It does however eliminate the tails in the contours in a way that is similar to the imposition of outside data sets. The two methods and broadbands give consistent results, as seen in table 1.

We used the sets of mock spectra to search for biases in our measurement of  $\alpha_{iso}$ . The mean value reconstructed for this quantity on individual mocks is  $1.002 \pm 0.007$ , suggesting that there are no significant biases in the determination of the BAO scale. Figure 17 shows the values and errors for the individual mocks along with that for the data. Both the measured value and its uncertainty for the data is typical of that found for individual sets of mock spectra.

## 5.2. Constraints on cosmological models

Our constraints on  $(D_A/r_s, H r_s)$  can be used to constrain the cosmological parameters. In a  $\Lambda$ CDM cosmology, apart from the pre-factors of  $H_0$  that cancel,  $D_A/r_s$  and  $H r_s$  evaluated at  $z = 2.3$  depend primarily on  $\Omega_M$  through  $r_s$  and on  $\Omega_\Lambda$  which, with  $\Omega_M$ , determines  $D_A$  and  $H$ . The sound horizon also depends on  $H_0$  (required to derive  $\Omega_\gamma$  from  $T_{CMB}$ ), on the effective number of neutrino species  $N_\nu$  (required to derive the radiation density from

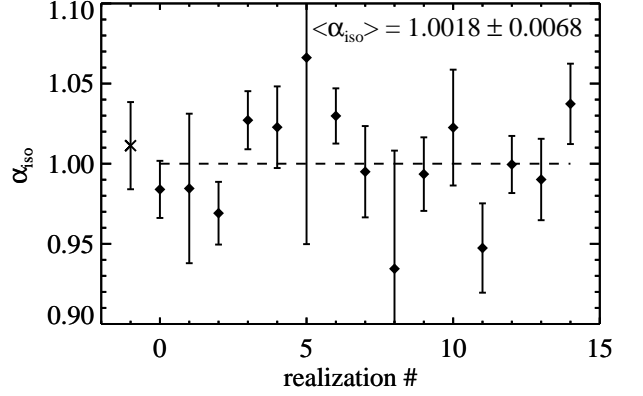


**Fig. 17.** The measurements of  $\alpha_{iso} (= \alpha_l = \alpha_r)$  for the 15 sets of mock spectra and for the data (realization=-1). The large errors for realization 5 and 8 are due to the very low significance of the BAO peak found on these two sets.

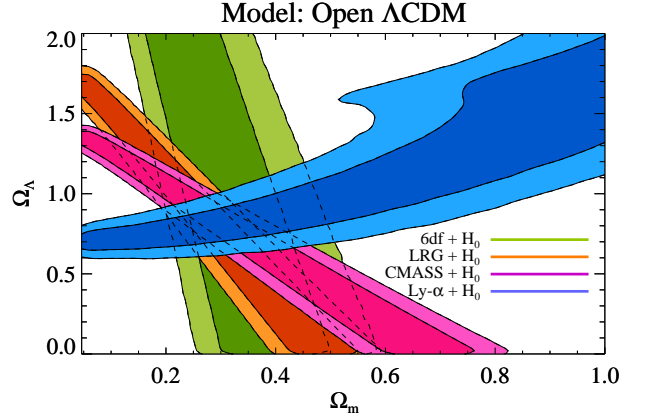


**Fig. 18.** Constraints on the matter and dark-energy density parameters  $(\Omega_M, \Omega_\Lambda)$  assuming a dark-energy pressure-density ratio  $w = -1$ . The blue regions are the one and two standard deviation constraints derived from our contours in figure 16 (method 2, broadband 24) combined with a measurement of  $H_0$  (Riess et al., 2011). Also shown are one and two standard deviation contours from lower redshift measurements of  $D_V/r_s$  (also combined with  $H_0$ ) at  $z = 0.11$  [6df: Beutler et al. (2011)],  $z = 0.35$  [LRG: Percival et al. (2010)] and  $z = 0.57$  [CMASS: Anderson et al. (2012)]. All constraints use a WMAP7 (Komatsu et al., 2011) prior on the baryon-to-photon ratio  $\eta$  but do not otherwise incorporate CMB results.

the photon density), and on the baryon-to-photon number ratio,  $\eta$  (required for the speed of sound).

Figure 18 shows the  $\Lambda$ CDM constraints on  $(\Omega_M, \Omega_\Lambda)$  derived from the contours in figure 16 combined with the most recent measurement of  $H_0$  (Riess et al., 2011). We use the contours for method 2 and the broadband of equation 24 which gives better fits to the data than the other method and broadband. The contours also assume  $N_\nu = 3$  and the WMAP7 value of  $\eta$  (Komatsu et al., 2011). Also shown are constraints from BAO measurements of  $D_V/r_s$  (Percival et al., 2010; Anderson et al., 2012; Beutler et al., 2011).

The Ly $\alpha$  contours are nicely orthogonal to the lower redshift  $D_V/r_s$  measurements, reinforcing the requirement of dark en-



**Table 1.** Results with the two methods and two broadband (equations 23 and 24). Columns 2 and 3 give the  $\chi^2$  for the fiducial model and for the model with the minimum  $\chi^2$ . Column 4 gives the best fit for  $\alpha_{iso}$  with the constraint ( $\alpha_t = \alpha_r \equiv \alpha_{iso}$ ). Column 5 gives  $Hr_s/[Hr_s]_{fid}$  with the  $2\sigma$  limits in parentheses. Column 6 gives the  $Hr_s/[Hr_s]_{fid}$  deduced by combining our data with that of WMAP7 (Komatsu et al., 2011) (see section 5.3).

| method & broadband | $\chi^2_{fid}/DOF$ | $\chi^2_{min}/DOF$ | $\alpha_{iso}$    | $Hr_s/[Hr_s]_{fid}$                      | $Hr_s/[Hr_s]_{fid}$<br>(with WMAP7) |
|--------------------|--------------------|--------------------|-------------------|------------------------------------------|-------------------------------------|
| Method 1 (24)      | 85.0/80            | 84.6/78            | $1.035 \pm 0.035$ | $0.876 \pm 0.049$ $(^{+0.188}_{-0.111})$ | $0.983 \pm 0.035$                   |
| Method 2 (24)      | 71.5/80            | 71.4/78            | $1.010 \pm 0.025$ | $0.954 \pm 0.077$ $(^{+0.152}_{-0.154})$ | $1.000 \pm 0.036$                   |
| Method 1 (23)      | 104.3/82           | 99.9/80            | $1.027 \pm 0.031$ | $0.869 \pm 0.044$ $(^{+0.185}_{-0.084})$ | $0.988 \pm 0.034$                   |
| Method 2 (23)      | 88.4/82            | 87.7/80            | $1.004 \pm 0.024$ | $0.994 \pm 0.111$ $(^{+0.166}_{-0.178})$ | $1.006 \pm 0.032$                   |

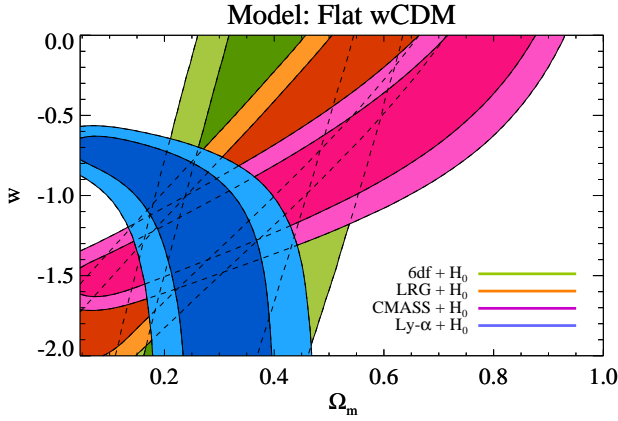


**Fig. 19.** As in figure 18 with constraints on the matter density parameter,  $\Omega_M$ , and dark-energy pressure-density ratio  $w$  assuming  $\Omega_M + \Omega_\Lambda = 1$ .

ergy from BAO data. In fact, our measurement is the only BAO measurement that by itself requires dark energy:  $\Omega_\Lambda > 0.5$ . This is because at  $z = 2.3$  the universe is strongly matter dominated and the  $\sqrt{\Omega_M}$  factor in  $H$  partially cancels the  $1/\sqrt{\Omega_M}$  in  $r_s$ , enhancing the importance of the  $\Omega_\Lambda$  dependence of  $H$ .

Figure 19 shows the constraints on  $(\Omega_M, w)$ ; where  $w$  is the dark-energy pressure-density ratio) assuming a flat universe:  $\Omega_k = 0$ . Our result is the only BAO measurement that by itself requires negative  $w$ . Our limit  $w < -0.6$  requires matter domination at  $z = 2.3$ .

$$\frac{\rho_{de}(z = 2.3)}{\rho_m(z = 2.3)} < 0.3 \left( \frac{\Omega_\Lambda/\Omega_M}{0.73/0.27} \right). \quad (25)$$

### 5.3. Constraints on $H(z)$

The contours in figure 16 give the measurements of  $Hr_s$  given in table 1. A measurement of the expansion rate deep in the matter-dominated epoch can be used to demonstrate the deceleration of the expansion at that time. Unfortunately, our data are not yet precise enough to do this. To make a more precise measurement of  $H(z = 2.3)$ , we must add further constraints to eliminate the long tails in figure 16. These tails correspond to models where  $1/H(z = 2.3)$  is increased (resp. decreased) with respect to the fiducial value while  $D_A(z = 2.3)$  is decreased (resp. increased). For flat models, this would imply a change in the mean of  $1/H$  (averaged up to  $z = 2.3$ ) that is opposite to that of the change in  $1/H(z = 2.3)$ , which requires a functional form  $H(z)$  that

strongly differs from the fiducial case. It is possible to construct models with this property by introducing significant non-zero curvature.

Because of the importance of curvature, the tails are eliminated once WMAP7 constraints (Komatsu et al., 2011) are included. This is done in figure 20 within the framework of non-flat models where the dark-energy pressure-density ratio,  $w(z)$ , is determined by two parameters,  $w_0$  and  $w_a$ :  $w(z) = w_0 + w_a z/(1 + z)$ . As expected, the WMAP7 results in this framework constrain  $D_A$  and  $1/H$  to migrate in roughly the same direction as one moves away from the fiducial model. Combining WMAP7 constraints with ours gives the values of  $H(z = 2.3)r_s$  given in the last column of table 1. For what follows, we adopt the mean of methods 1 and 2 that use the more flexible broadband of equation (24):

$$\frac{H(z = 2.3)r_s}{[H(z = 2.3)r_s]_{fid}} = 0.992 \pm 0.035. \quad (26)$$

The precision on  $H$  is now sufficient to study the redshift evolution of  $H(z)$ .

The fiducial model has  $r_s = 152.76$  Mpc and  $H(z = 2.3) = 3.23H_0$ ,  $H_0 = 70 \text{ km s}^{-1} \text{ Mpc}^{-1}$ . These results produce

$$\frac{H(z = 2.3)r_s}{1 + z} = (1.036 \pm 0.036) \times 10^4 \text{ km s}^{-1}. \quad (27)$$

or equivalently

$$\frac{H(z = 2.3)}{1 + z} = (67.8 \pm 2.4) \text{ km s}^{-1} \text{ Mpc}^{-1} \left( \frac{152.76 \text{ Mpc}}{r_s} \right). \quad (28)$$

This number can be compared with the measurements of  $H(z)$  at lower redshift shown in table 2 and figure 21. Other than those of  $H_0$ , the measurements that we use can be divided into two classes: those (like ours) that use  $r_s$  as the standard of length and those that use  $c/H_0$  as the standard of length.

The comparison with our measurement is simplest with BAO-based measurements that use  $r_s$  as the standard of length and therefore measure  $H(z)r_s$  (as is done here). The first attempt at such a measurement was made by Gaztañaga et al. (2009), a result debated in subsequent papers by Miralda-Escudé (2009), Yoo & Miralda-Escudé (2010), Kazin et al. (2010), and Cabré & Gaztañaga (2011). Here, we use four more recent measurements. Chuang & Wang (2012) and Xu et al. (2012) studied the SDSS DR7 LRG sample and decomposed the BAO peak into radial and angular components, thus extracting directly  $Hr_s$  and  $D_A/r_s$ . Blake et al. (2012) and Reid et al. (2012) took a more indirect route. They first used the angle-averaged peak position to derive  $D_V(z)/r_s = ((1 + z)^2 D_A^2 cz H^{-1})/r_s$ . They then studied



**Table 2.** Recent measurements of  $H(z)/(1+z)$ . The BAO-based measurements use  $r_s = 152.76$  Mpc as the standard of length and are shown as the filled circles in figure 21. The quoted uncertainties in  $H(z)$  do not include uncertainties in  $r_s$  which are expected to be negligible,  $\approx 1\%$  (Komatsu et al., 2011). The measurements of Blake et al. (2011b) use supernova data and therefore measure  $H(z)$  relative to  $H_0$ . We quote the results they obtain without assuming a flat universe and plot them as the open green circles in figure 21 assuming  $h = 0.7$ .

| $z$  | $H(z)/(1+z)$<br>$\text{km s}^{-1}\text{Mpc}^{-1}$ | method    | reference            |
|------|---------------------------------------------------|-----------|----------------------|
| 2.3  | $66.5 \pm 7.4$                                    | BAO       | this work            |
| 2.3  | $67.8 \pm 2.4$                                    | BAO+WMAP7 | this work            |
| 0.35 | $60.8 \pm 3.6$                                    | BAO       | Chuang & Wang (2012) |
| 0.35 | $62.5 \pm 5.2$                                    | BAO       | Xu et al. (2012)     |
| 0.57 | $58.8 \pm 2.9$                                    | BAO + AP  | Reid et al. (2012)   |
| 0.44 | $57.4 \pm 5.4$                                    | BAO + AP  | Blake et al. (2012)  |
| 0.60 | $54.9 \pm 3.8$                                    |           |                      |
| 0.73 | $56.2 \pm 4.0$                                    |           |                      |
| 0.2  | $(1.11 \pm 0.17)H_0$                              | AP + SN   | Blake et al. (2011b) |
| 0.4  | $(0.83 \pm 0.13)H_0$                              |           |                      |
| 0.6  | $(0.81 \pm 0.08)H_0$                              |           |                      |
| 0.8  | $(0.83 \pm 0.10)H_0$                              |           |                      |
| 0    | $73.8 \pm 2.5$                                    |           | Riess et al. (2011)  |

the Alcock-Paczynski effect on the broadband galaxy correlation function to determine  $D_A(z)H(z)$ . Combining the two measurements yielded  $H(z)r_s$ .

It is evident from comparing our  $H(z)$  measurement (filled red circle in figure 21) to the other BAO-based measurements (other filled circles) that  $H(z)/(1+z)$  decreases between  $z = 2.3$  and  $z = 0.35 - 0.8$ . To demonstrate deceleration quantitatively, we fit the eight BAO-based values of  $H(z)$  in table 2 to the  $\Lambda$ CDM form  $H(z) = H_0(\Omega_\Lambda + \Omega_M(1+z)^3 + (1 - \Omega_\Lambda - \Omega_M)(1+z)^2)^{1/2}$ . Marginalizing over  $\Omega_\Lambda$  and  $H_0$  we find

$$\frac{[H(z)/(1+z)]_{z=2.3}}{[H(z)/(1+z)]_{z=0.5}} = 1.17 \pm 0.05, \quad (29)$$

clearly indicating deceleration between  $z = 2.3$  and  $z = 0.5$ . This measurement is in good agreement with the fiducial value of 1.146. We emphasize that this result is independent of  $r_s$ , assuming only that the BAO-peak position is redshift-independent in comoving coordinates. The result also does not assume spatial flatness.

To map the expansion rate over the full range  $0 < z < 2.3$ , we must adopt the fiducial value of  $r_s$  and compare the resulting  $H(z)$  with  $H_0$  and with other BAO-free measurements. Besides the  $H_0$  measurement of Riess et al. (2011), we use the WiggleZ analysis combining their Alcock-Paczynski data with distant supernova data from the Union-2 compilation (Amanullah et al., 2010). The supernova analysis does not use the poorly known mean SNIa luminosity, so the SNIa Hubble diagram gives the luminosity distance in units of  $H_0^{-1}$ ,  $D_L(z)H_0$ . Combining this result with the Alcock-Paczynski measurement of  $D_A(z)H(z)$  yields  $H(z)/H_0$ . The values are given in table 2.

We fit all the data in table 2 (filled and open circles in figure 21) to the  $\Lambda$ CDM form of  $H(z)$ . This yields an estimate of the redshift of minimum  $H(z)/(1+z)$

$$z_{d-a} = 0.82 \pm 0.08 \quad (30)$$

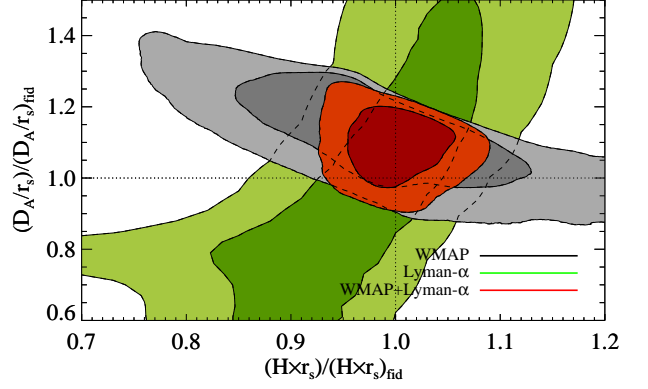


**Fig. 20.** Constraints on  $(D_A/r_s, r_s H)_{z=2.3}$  within the framework of  $\Lambda$ CDM models. The green contours are our  $1\sigma$  and  $2\sigma$  constraints using method 2 and broadband (24). The gray contours are the  $1\sigma$  and  $2\sigma$  constraints from WMAP7 (Komatsu et al., 2011). The red contours show the combined constraints.

which compares well with the fiducial value:  $z_{d-a} = (2\Omega_\Lambda/\Omega_M)^{1/3} - 1 = 0.755$ .

In this analysis, we have not used two other sources of information on  $H(z)$  at high redshift. The first use high-redshift type Ia supernovae to probe the era where the universe transitions from deceleration to acceleration (e.g., Riess et al. (2004, 2007)). The data of Riess et al. (2007) (plotted as the open squares in figure 21)) yielded useful measurements up to  $z \sim 1.1$ . However, this data yields constraints on  $H(z)$  that are weaker than those of BAO-based methods because of the need to differentiate the distance-redshift relation. Moreover, these inferences of  $H(z)$  assume spatial flatness. Fitting the SNe data to a model with an evolving deceleration parameter  $q(z) = q_0 + (dq/dz)_0 z$  and assuming flatness, Riess et al. (2007) and Riess et al. (2004) were able to demonstrate that  $(dq/dz)_0 > 0$ , i.e. a negative 3rd-derivative of  $a(t)$ . However, we point out that in a more general  $q(z)$  model, the demonstration that  $dq/dz > 0$  at low redshift is not equivalent to a demonstration that  $\ddot{a}$  becomes negative in the past.

Another approach to determining  $H(z)$  uses the evolution of stellar populations as a clock to infer  $dt/dz$  (Stern et al., 2010; Moresco et al., 2012). This method yields results that are consistent with  $\Lambda$ CDM expectations, but the uncertainties (statistical and systematic) are larger than those of the determinations in Table 2, so we have not plotted them in figure 21.

## 6. Conclusions

In this paper, we have presented the first observation of the BAO peak using the Ly $\alpha$  forest. It represents both the first BAO detection deep in the matter dominated epoch and the first to use a tracer of mass that is not galactic. The results are consistent with concordance  $\Lambda$ CDM, and require, by themselves, the existence of dark energy. Combined with CMB constraints, we deduce the expansion rate at  $z = 2.3$  and demonstrate directly the sequence of deceleration and acceleration expected in dark-energy dominated cosmologies. These results have been confirmed with higher precision by Slosar et al. (2013) using the same underlying DR9 data set but more aggressive data cuts and a more nearly optimal statistical method.

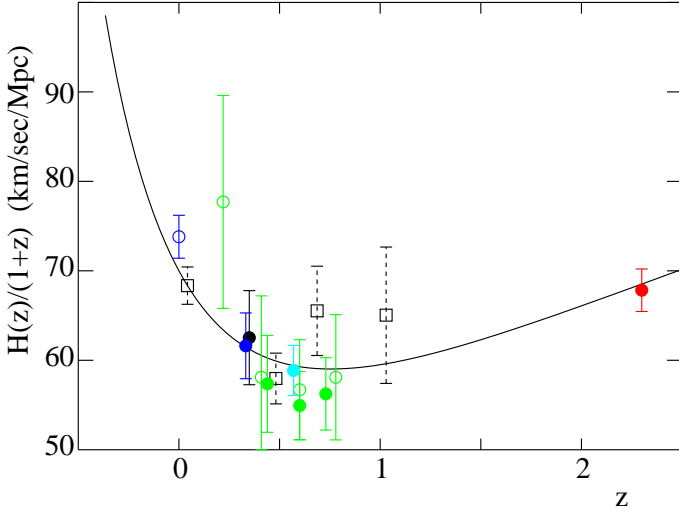


**Fig. 21.** Measurements of  $H(z)/(1+z)$  vs  $z$  demonstrating the acceleration of the expansion for  $z < 0.8$  and deceleration for  $z > 0.8$ . The BAO-based measurements are the filled circles: [this work: red], [Xu et al. (2012): black] [Chuang & Wang (2012): blue], [Reid et al. (2012), cyan], and [Blake et al. (2012): green]. The open green circles are from WiggleZ (Blake et al., 2011b) Alcock-Paczynski data combined with supernova data yielding  $H(z)/H_0$  (without the flatness assumption) plotted here assuming  $H_0 = 70 \text{ km s}^{-1} \text{ Mpc}^{-1}$ . The open blue circle is the  $H_0$  measurement of Riess et al. (2011). The open black squares with dashed error bars show the results of Riess et al. (2007) which were derived by differentiating the SNIa Hubble diagram and assuming spatial flatness. (For visual clarity, the Riess et al. (2007) point at  $z = 0.43$  has been shifted to  $z = 0.48$ .) The line is the  $\Lambda$ CDM prediction for  $(h, \Omega_M, \Omega_\Lambda) = (0.7, 0.27, 0.73)$ .

BOSS continues to acquire data and will eventually produce a quasar sample three times larger than DR9. We can thus expect improved precision in our measurements of distances and expansion rates, leading to improved constraints on cosmological parameters. The Ly $\alpha$  forest may well be the most practical method for obtaining precise  $D_A(z)$  and  $H(z)$  measurements at  $z > 2$ , thanks to the large number of independent density measurements per quasar. It is reassuring that the first sample large enough to yield a detection of BAO produces a signal in good agreement with expectations. In the context of BAO dark energy constraints, high redshift measurements are especially valuable for breaking the degeneracy between curvature and the equation of state history. More generally, however, by probing an epoch largely inaccessible to other methods, BAO in the Ly $\alpha$  forest have the potential to reveal surprises, which could provide critical insights into the origin of cosmic acceleration.

*Acknowledgements.* We thank Carlos Allende Prieto, Ashley Ross and Uros Seljak for stimulating discussions and Adam Riess for providing the data points of Riess et al. (2007) in figure 21.

Funding for SDSS-III has been provided by the Alfred P. Sloan Foundation, the Participating Institutions, the National Science Foundation, and the U.S. Department of Energy Office of Science. The SDSS-III web site is <http://www.sdss3.org/>.

The French Participation Group of SDSS-III was supported by the Agence Nationale de la Recherche under contract ANR-08-BLAN-0222.

The research leading to these results has received funding from the European Union Seventh Framework Programme (FP7/2007-2013) under grant agreement no. [PIIF-GA-2011-301665].

SDSS-III is managed by the Astrophysical Research Consortium for the Participating Institutions of the SDSS-III Collaboration including the University of Arizona, the Brazilian Participation Group, Brookhaven National Laboratory,

University of Cambridge, Carnegie Mellon University, University of Florida, the French Participation Group, the German Participation Group, Harvard University, the Instituto de Astrofísica de Canarias, the Michigan State/Notre Dame/JINA Participation Group, Johns Hopkins University, Lawrence Berkeley National Laboratory, Max Planck Institute for Astrophysics, Max Planck Institute for Extraterrestrial Physics, New Mexico State University, New York University, Ohio State University, Pennsylvania State University, University of Portsmouth, Princeton University, the Spanish Participation Group, University of Tokyo, University of Utah, Vanderbilt University, University of Virginia, University of Washington, and Yale University.

## Appendix A: Mock quasar spectra

We have produced mock spectra in order to tune the analysis procedure and to study statistical uncertainties and systematic effects in the measured correlation function.

In some galaxy clustering studies (e.g. Anderson et al. (2012)) the covariance matrix of the measured correlation function is obtained from mock data sets. In this case, it is crucial to have very realistic mocks with the right statistics.

In order to do so, we would need to generate several realizations of hydrodynamical simulations, with a large enough box to cover the whole survey (several  $\text{Gpc}^3$ ) and at the same time have a good enough resolution to resolve the Jeans mass of the gas (tenths of kpc). This type of simulations are not possible to generate with current technology, but luckily in this study the covariance matrix is obtained from the data itself, and the mock data sets are only used to test our analysis and to study possible systematic effects.

In the last few years there have been several methods proposed to generate simplified mock Lyman- $\alpha$  surveys by combining Gaussian fields and nonlinear transformations of the field (Le Goff et al., 2011; Greig et al., 2011; Font-Ribera et al., 2012a). In this study we used a set of mocks generated using the process described in Font-Ribera et al. (2012a), the same method used in the first publication of the Lyman- $\alpha$  correlation function from BOSS (Slosar et al., 2011).

The mock quasars were generated at the angular positions and redshifts of the BOSS quasars. The unabsorbed spectra (continua) of the quasars were generated using the Principal Component Analysis (PCA) eigenspectra of Suzuki et al. (2005), with amplitudes for each eigenspectrum randomly drawn from Gaussian distributions with sigma equal to the corresponding eigenvalues as published in Suzuki (2006) table 1. A detailed description will be provided by Bailey et al. (in preparation), accompanying a public release of the mock catalogs.

We generated the field of transmitted flux fraction,  $F$ , that have a  $\Lambda$ CDM power spectrum with the fiducial parameters

$$(\Omega_M, \Omega_\Lambda, \Omega_b h^2, h, \sigma_8, n_s)_{\text{fid}} = (0.27, 0.73, 0.0227, 0.7, 0.8, 0.97) \quad (\text{A.1})$$

where  $h = H_0/100 \text{ km s}^{-1} \text{ Mpc}^{-1}$ . These values produce a fiducial sound horizon of

$$r_{s,\text{fid}} = 152.76 \text{ Mpc} . \quad (\text{A.2})$$

Here, we use the parametrized fitting formula introduced by McDonald (2003) to fit the results of the power spectrum from several numerical simulations,

$$P_F(k, \mu_k) = b_\delta^2 (1 + \beta \mu_k^2)^2 P_L(k) D_F(k, \mu_k) , \quad (\text{A.3})$$

where  $\mu_k = k_{\parallel}/k$  is the cosine of the angle between  $\mathbf{k}$  and the line of sight,  $b_\delta$  is the density bias parameter,  $\beta$  is the redshift distortion parameter,  $P_L(k)$  is the linear matter power spectrum,

and  $D_F(k, \mu_k)$  is a non-linear term that approaches unity at small  $k$ . This form of  $P_F$  is the expected one at small  $k$  in linear theory, and provides a good fit to the 3-D Ly $\alpha$  observations reported in Slosar et al. (2011). We do not generate a density and a velocity field, but directly create the Ly $\alpha$  forest absorption field instead, with the redshift distortions being directly introduced in the input power spectrum model of equation (A.3), with the parameter  $\beta$  that measures the strength of the redshift distortion.

To model the evolution of the forest with redshift,  $b_\delta$  varies with redshift according to  $b_\delta = 0.14[(1+z)/3.25]^{1.9}$  (McDonald et al., 2006). The redshift distortion parameter is given a fixed value of  $\beta_F = 1.4$ . The non-linear correction factor  $D(k, \mu_k)$  is taken from McDonald (2003). The flux field was constructed by generating Gaussian random fields  $g$  with an appropriately chosen power spectrum (Font-Ribera et al., 2012a) to which the log-normal transformation  $F = \exp(-ae^{v\delta})$  is applied (Coles & Jones, 1991; Bi et al., 1992; Gnedin & Hui, 1996). Here  $a$  and  $v$  are free parameters chosen to reproduce the flux variance and mean transmitted flux fraction (McDonald et al., 2006).

DLA's were added to the spectra according to the procedure described in Font-Ribera et al. (2012b).

Finally, the spectra were modified to include the effects of the BOSS spectrograph point spread function (PSF), readout noise, photon noise, and flux miscalibration.

Fifteen independent realizations of the BOSS data were produced and analyzed with the same procedures as those for the real data.

We used the mock spectra to understand how our analysis procedure modifies the correlation function. Figure A.1 shows the average over 15 mocks of the reconstructed quadrupole and monopole using methods 1 and 2 (sections 3.1 and 3.2) and that reconstructed with the true continuum. The monopole and quadrupole for the two methods have a general shape that follows that found with the true continuum including the position of the BAO peak. However, both methods produce a monopole that becomes negative for  $60 \text{ h}^{-1}\text{Mpc} < r < 100 \text{ h}^{-1}\text{Mpc}$  while the true monopole remains positive for all  $r < 130 \text{ h}^{-1}\text{Mpc}$ . As discussed in section 3.2, this result is due to the continuum estimation of the two methods which introduced negative correlations. For both methods, however, the BAO peak remains visible with a deviation above the “broadband” correlation function that is hardly affected by the distortion.

Figure A.2 presents  $\xi_0(r)$  and  $\xi_2(r)$  found with the data, along with the mean of 15 mocks. The figure demonstrates that our mocks do not perfectly reproduce the data. In particular, for  $r < 80 \text{ h}^{-1}\text{Mpc}$ , the monopole is underestimated and the quadrupole overestimated. Since we use only peak positions to extract cosmological constraints, we only use the mocks qualitatively to search for possible systematic problems in extracting the peak position.

## Appendix B: Results for a Fiducial BOSS Ly $\alpha$ Forest Sample

The spectra analyzed here are all available through SDSS DR9 (Ahn et al., 2012), and the DR9 quasar catalog is described by Pâris et al. (2012). A Ly $\alpha$  forest analysis requires many detailed choices about data selection and continuum determination. To aid community analyses and comparison of results from different groups, Lee et al. (2012b) has presented a fiducial BOSS Ly $\alpha$  forest sample that uses constrained PCA continuum determination (Lee et al., 2012a) and reasonable choices of masks

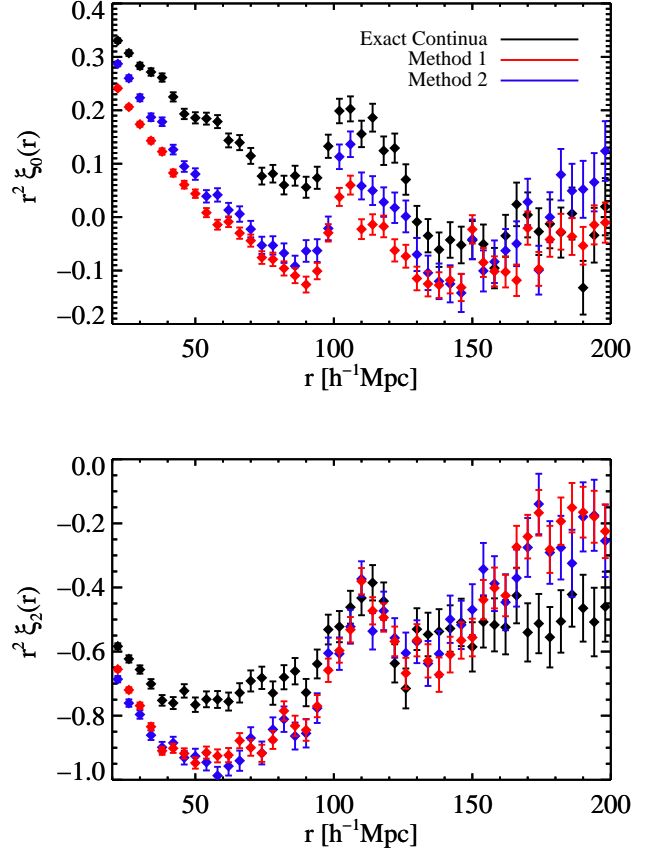


**Fig. A.1.** The effect of the continuum estimation procedure on the correlation function found with the mock spectra. The black dots are the average of monopole and quadrupole obtained with the 15 sets using the exact continua. The blue (red) dots show those obtained with the continuum estimation of method 1 (method 2) as described in section 3.1 (3.2).

for DLAs, BALs, and data reduction artifacts. Both the data selection and the continuum determination differ from those used here. Figure B.1 compares the Method 2 correlation function from this paper’s analysis to that obtained by applying the Method 2 weights and correlation measurement code directly to the continuum-normalized spectra of the fiducial Lee et al. sample. The good agreement in this figure, together with the good agreement between our Method 1 and Method 2 results, demonstrates the robustness of the BAO measurement, and the more general correlation function measurement, to the BOSS DR9 data.

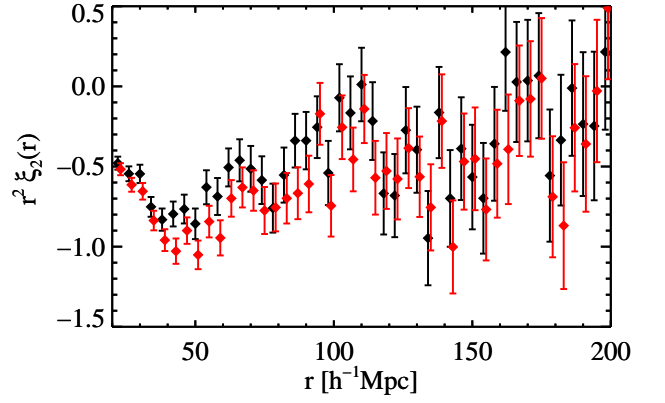
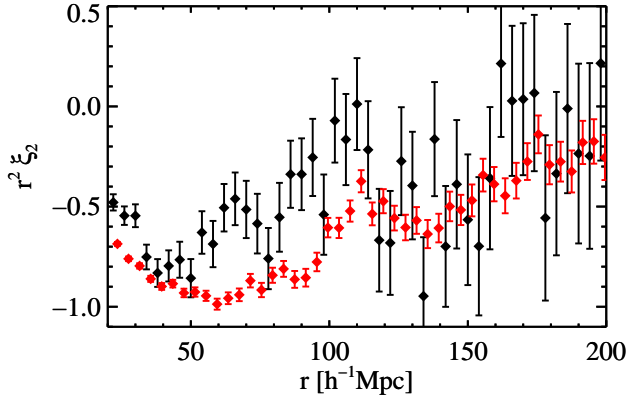
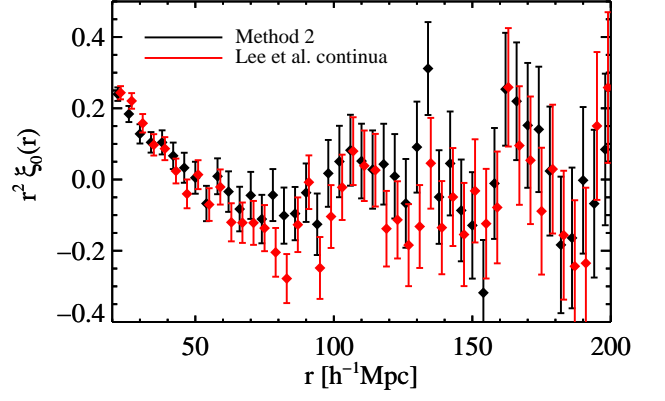
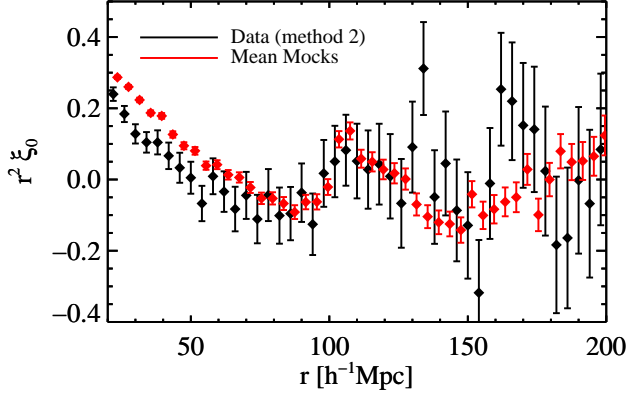


**Fig. A.2.** Comparison of the correlation function for the mock spectra and that for the data. The red dots show the mean of the 15 sets of mock spectra and the black dots show the data.

**Fig. B.1.** Comparison of the monopole and quadrupole correlation functions for the sample used here (black dots) and for the sample and continua of Lee et al. (2012b) (red dots).

## References

- Abazajian K.N., J.K. Adelman-McCarthy, M.S. Agüeros et al. 2009, *ApJS*, 182, 543
- Ahn, C.P., R. Alexandroff, C. Allende Prieto et al. 2012, *ApJS*, 203, 21
- Alcock, C. & B. Paczynski 1979, *Nature*, 281, 358
- Amanullah, R. et al. 2010, *ApJ*, 716, 712
- Anderson, L., E. Aubourg, S. Bailey et al. 2012, *MNRAS*, 427, 3435
- Bailey, S. et al. 2012, in preparation
- Becker, R.H., R.L. White & D.J. Helfand 1995, *ApJ*, 450, 559B
- Beutler F. et al. 2011, *MNRAS*, 416, 3017
- Bi, H.G., G. Börner & Y.Chu 1992, *A&A*, 266, 1
- Blake C. et al. 2011, *MNRAS*, 415, 2892
- Blake C. et al. 2011, *MNRAS*, 418, 1725
- Blake C. et al. 2012, *MNRAS*, 425, 405
- Blanton, M.R., H. Lin, R. H. Lupton et al. 2003, *AJ*, 125, 2276
- Bolton A. et al. 2012, *AJ*, 144, 144
- Bovy, J. et al. 2011, *ApJ*, 729, 141
- Bovy, J. et al. 2012, *ApJ*, 749, 41
- Cabré, A. & E. Gaztañaga 2011, *MNRAS*, 412, L98
- Cauci, S., S. Colombi, C. Pichon et al. 2008, *MNRAS*, 386, 211
- Cen R., Miralda-Escudé J., Ostriker J. P., Rauch M. 1994, *ApJ*, 437, L9
- Chuang, Chia-Hsun & Yun Wang 2012, *MNRAS*, 426, 226
- Cole, S. et al. 2005, *MNRAS*, 362, 505
- Coles, P. & B. Jones. 1991, *MNRAS*, 248, 1
- Croft, R. et al. 1997, *ApJ*, 488, 532
- Croft, R. et al. 1998, *ApJ*, 495, 44
- Croft, R.A.C., et al. 1999, *ApJ*, 520, 1
- Croft, R.A.C., D. Weinberg, M. Bolte, et al. 2002, *ApJ*, 581, 20
- Dawson, K., D. Schlegel, C. Ahn et al. 2013, *AJ*, 145, 10
- de Bernardis, P., P. A. R. Ade, J. J. Bock, et al. 2000, *Nature*, 404, 955
- Eisenstein D. J., Zehavi, I., Hogg, D.W. et al. 2005, *ApJ*, 633, 560
- Eisenstein, D.J. 2007, *ApJ*, 664, 675
- Eisenstein, D.J. et al. 2011, *AJ*, 142, 72
- Efron, B. & G. Gong 1983, *The American Statistician*, 37, 36
- Font-Ribera, A., P. McDonald & J. Miralda Escudé 2012, *J. Cosmology Astropart. Phys.*, 01, 001
- Font-Ribera, A. & Miralda-Escud, J. 2012, *J. Cosmology Astropart. Phys.*, 07, 028
- Fukugita, M., Ichikawa, T., Gunn, J. E., et al. 1996, *AJ*, 111, 1748
- Gallerani, S., F. S. Kitaura & A. Ferrara 2011, *MNRAS*, 413L, 6
- Gaztañaga, E., A. Cabré & L. Hui(2009), *MNRAS*, 399, 1663
- Gnedin, N. & L. Hui 1996, *ApJ*, 472 L73
- Greig, B., J. Bolton, J. Wyithe & B. Stuart 2011, *MNRAS*, 418, 1980
- Gunn, J.E., et al. 1998, *AJ*, 116, 3040
- Gunn, J.E., et al. 2006, *AJ*, 131, 2332
- Hamilton, A.J.S. 1992, *ApJ*, 385L, 5
- Hernquist L., Katz N., Weinberg D. H., Miralda-Escudé J. 1996, *ApJ*, 457, L51
- Kazin, E. A., M. R. Blanton, R. Scoccimarro et al. 2010, *ApJ*, 719, 1032
- Kirkpatrick, J.A., D. J. Schlegel, N. P. Ross, et al., 2011, *AJ*, 743, 125
- Kitaura, F.-S., S. Gallerani & A. Ferrara 2012, *MNRAS*, 420, 61
- Komaatsu, E. et al. 2011, *ApJS*, 192, 18
- Lawrence, A., S.J. Warren, O. Almaini et al. 2007, *MNRAS*, 379, 1599
- Le Goff, J. M. et al. 2011, *A&A*, 534, 135
- Lee, K.-G., Suzuki, N., & Spergel, D. N. 2012a, *AJ*, 143, 51
- Lee, K.-G., Bailey, S., Bartsch, L. E., et al. 2012b, *arXiv:1211.5146*
- Martin, D.C., J. Fanson, D. Schiminovich et al. 2005, *ApJ*, 619, L1
- McDonald, P. et al. 2000, *ApJ*, 543, 1
- McDonald, P. 2003, *ApJ*, 585, 34
- McDonald, P., U. Seljak, D.J. Schlegel et al. 2006, *ApJS*, 163, 80
- McDonald, P. & D. Eisenstein 2007, *Phys. Rev. D*, 76, 063009
- McQuinn, M. & M. White 2011, *MNRAS*, 415, 2257
- Mehta, K.T., A. Cuesta, X. Xu et al. 2012, *MNRAS*, 427, 2168
- Miralda-Escudé J., Cen R., Ostriker J. P., Rauch M. 1996, *ApJ*, 471, 582
- Miralda-Escudé J. (2009), *arXiv:0901.1219*
- Moresco, M., A. Cimatti, R. Jimenez et al. 2012, *J. Cosmology Astropart. Phys.*, 006, 1208
- Noterdaeme, P., P. Petitjean, W.C. Carithers et al. 2012, *A&A*, 547, L1
- Nusser, A. & M. Haehnelt 1999, *MNRAS*, 303, 179
- Padmanabhan, N., Schlegel, D. J., Finkbeiner, D. P., et al. 2008, *ApJ*, 674, 1217
- Padmanabhan, N. et al. 2009, *Phys. Rev. D*, 79, 3523
- Padmanabhan, N., X. Xu, D.J. Eisenstein et al. 2012, *MNRAS*, 427, 2132
- Palanque-Delabrouille, N., C. Yèche, A. D. Myers et al. 2011, *A&A*, 530, 122
- Pâris, I., Petitjean, P., Rollinde, et al. 2011, *A&A*, 530, 50
- Pâris, I., P. Petitjean, E. Aubourg et al. 2012, *A&A*, 548, 66
- Percival, W.J., B.A. Reid, D.J. Eisenstein et al. 2010, *MNRAS*, 401, 2148
- Petitjean P., Mückert J. P., Kates R. E. 1995, *A&A*, 295, L9
- Pichon, C., J. L. Vergely, E. Rollinde et al. 2001, *MNRAS*, 326, 597
- Pier, J. R., Munn, J. A., Hindsley, R. B., et al. 2003, *AJ*, 125, 1559
- Pieri, M. M. et al. 2010, *ApJ*, 724, L69
- Reid, B.A., L. Samushia, M. White et al. 2012, *MNRAS*, 426, 2719
- Richards, G.T. et al. 2009, *ApJS*, 180, 67
- Riess, A.G., L.-G. Strolger, J. Tonry et al. 2004, *ApJ*, 607, 665
- Riess, A.G., L.-G. Strolger, S. Casertano et al. 2007, *ApJ*, 659, 98
- Riess, A.G., L. Macri, S. Casertano et al. 2011, *ApJ*, 730, 119
- Ross, N.P. et al. 2012, *ApJS*, 199, 3
- Seo, H.-J., S. Ho, M. White et al. 2012, *ApJ*, 761, 13
- Slosar, A. et al. 2011, *J. Cosmology Astropart. Phys.*, 09, 001
- Slosar, A. et al. (2013), *arXiv:1301.3459*
- Smee, S., J.E. Gunn, A. Uomoto et al. 2012, *arXiv:1208.2233*
- Smith, J. A., Tucker, D. L., Kent, S., et al. 2002, *AJ*, 123, 2121
- Stern, D. et al. 2010, *J. Cosmology Astropart. Phys.*, 02, 008
- Stoughton, C., Lupton, R. H., Bernardi, M., et al. 2002, *AJ*, 123, 485
- Suzuki, N., D. Tytler, D. Kirkman et al. 2005, *ApJ*, 618, 592
- Suzuki, N. 2006, *ApJS*, 163, 110
- Theuns T., Leonard A., Efstathiou, G., Pearce F.R., Thomas, P.A. 1998, *MNRAS*, 301, 478
- Viel, M., M.G. Haehnelt & V. Springel 2004, *MNRAS*, 354, 684
- Weinberg, D.H. et al. 1998, *ASPC*, 148, 21
- Weinberg, D.H., J. J. Mortonson, D. J. Eisenstein et al. 2012, *arXiv:1201.2434*
- White, M. 2003, *The Davis Meeting On Cosmic Inflation*. 2003 March 22-25, Davis CA., p.18
- Worseck, G. & L. Wisotzki 2006, *A&A*, 450, 495; A. Lidz et al. (2010) *ApJ*, 718, 199
- Xu, X., Cuesta, A.J., N. Padmanabhan et al. 2012, *arXiv:1206.6732*
- Yèche, C., P. Petitjean, J. Rich, et al. 2009, *A&A*, 523, A14
- Yoo, J. & J. Miralda-Escudé 2010, *Phys. Rev. D*, 82, 3527
- York, D. G. et al. (SDSS Collaboration) 2000, *AJ*, 120, 1579
- Zhang, Y., Anninos P., Norman M. L. 1995, *ApJ*, 453, L57